Torsional Alfvén waves in a dipolar magnetic field: experiments and simulations

Zahia Tigrine, Henri-Claude Nataf, Nathanaël Schaeffer, Philippe Cardin, Franck Plunian

submitted to *Geophys. J. Int.*

Torsional Alfvén waves in a dipolar magnetic field: experiments and simulations

Z. Tigrine[1,2], H.-C. Nataf [1], N. Schaeffer[1], P. Cardin[1] and F. Plunian[1]

[1] *Univ Grenoble Alpes, Univ Savoie Mont Blanc, CNRS, IRD, IFSTTAR, ISTerre, 38000 Grenoble, France*

[2] *University of Sciences and Technology Houari Boumediene, 16111, Algiers, Algeria.*

SUMMARY

The discovery of torsional Alfvén waves (geostrophic Alfvén waves) in the Earth's core (Gillet et al. 2010) calls for a better understanding of their properties. We present the first experimental observations of torsional Alfvén waves, performed in the DTS-Ω set-up. In this set-up, 50L of liquid sodium (magnetic Prandtl number $Pm = 7.4 \times 10^{-6}$) are confined between an inner sphere ($r_i = 74$ mm) and an outer shell ($r_o = 210$ mm). The inner sphere houses a permanent magnet, imposing a vertically aligned dipolar magnetic field ($B_{max} = 345$ mT). Both the inner sphere and the outer shell can rotate around the vertical axis. Alfvén waves are triggered by a sudden and short rotation (jerk) of the inner sphere. We study the propagation of these waves when the fluid is initially at rest, and when it spins at a rotation rate up to 15 Hz. The waves produce an azimuthal magnetic field, which we measure at different radii inside the fluid with magnetometers installed in a sleeve. We also record the electric potential signature on the outer shell at several latitudes. Besides, we probe the associated azimuthal velocity field using ultrasound Doppler velocimetry. With a 15 Hz rotation rate, and because of the radial decay of the magnetic field intensity, the dynamical regimes we achieve are characterized by dimensionless numbers in the following ranges: Lundquist number $0.5 < Lu < 16$, Lehnert number $0.01 < Le < 0.3$, Rossby number $Ro \sim 0.1$.

We observe that the magnetic signal propagates away from the inner sphere, damped by magnetic diffusion. Rotation affects the magnetic signature in a subtle way. Its effect is more pronounced on the surface electric potentials, which are sensitive to the actual fluid velocity of the wave. The ultrasound Doppler probes provide the first experimental measurement of the fluid velocity of an Alfvén wave.

To complement these observations, we ran numerical simulations, using the XSHELLS pseudo-spectral code with parameters as close as possible to the experimental ones. The synthetic magnetic and electric signals match our measurements. The meridional snapshots of the synthetic azimuthal velocity field reveal the formation of geostrophic cylinders expected for torsional Alfvén waves, and the excitation of inertial modes for abrupt jerks of the inner sphere. In the absence of rotation, inertial effects become dominant both in the experiments and in the simulations. The resulting non-linear regimes reveal the formation of an equatorial sheet with a mushroom-shape cross-section.

We establish scaling laws for the magnetic and kinetic energies of Alfvén waves with and without rotation. In both cases, we find that the magnetic energy E_M saturates at a level proportional to Rm_{jerk}^2, where $Rm_{jerk} = U_{jerk} r_o/\eta$ is the magnetic Reynolds number built with the maximum azimuthal velocity of the inner sphere during the jerk. The E_K^{max}/E_M^{max} ratio (where E_K^{max} is the maximum kinetic energy), close to 1 for very short rotation, increases linearly with the jerk duration.

Key words: Core – Dynamo: theories and simulations – Planetary interiors

1 INTRODUCTION

The discovery of torsional Alfvén waves in the liquid core of the Earth (Gillet et al. 2010) represents a milestone in the exploration of the Earth's deep interior. The presence of a dynamo-produced magnetic field in the electrically conducting liquid iron core allows for the propagation of hydromagnetic waves (Alfvén 1942). The Lorentz force is the restoring force for these waves, which are solutions of the coupled system of the Navier-Stokes equation and the magnetic induction equation.

In a rotating system, such as a planetary core, the Coriolis force inhibits motions that vary along the rotation axis. This is the Proudman-Taylor theorem. Therefore, rotation inhibits Alfvén waves that violate the Proudman-Taylor constraint. In a sphere, axisymmetric motions that are purely az-

imuthal and invariant along the rotation axis obey the Proudman-Taylor's constraint. They are called geostrophic motions. Geostrophic Alfvén waves are thus favored in a rotating system (Lehnert 1954b; Braginsky 1970; Jault and Finlay 2015). They are called torsional Alfvén waves or torsional waves for short.

Gillet et al. (2010) found convincing evidence for such waves in the Earth's core. The secular variation of the magnetic field at the surface of the Earth reflects the motions that take place at the surface of the liquid core. Core flows reconstructed from the observed secular variation reveal azimuthal motions on axi-centered cylinders that propagate across the liquid core. It takes them about 4 years to cross the core. The velocity of Alfvén waves being proportional to the intensity of the magnetic field, these observations yield a crucial information on the intensity of the magnetic field inside the liquid core. They also provide a remarkable explanation for the variations of the length-of-day observed at periods of about 6 years (Gillet et al. 2010, 2015).

Despite their importance, torsional Alfvén waves have never been explored in laboratory experiments. In this article, we present observations of torsional Alfvén waves triggered in the DTS-Ω liquid sodium experiment. We conduct numerical simulations of these waves, using parameters as close as possible to the experimental ones, as already done for sustained turbulence in this set-up by Kaplan et al. (2018).

Only a few laboratory experiments have been performed to study Alfvén waves in liquid metals. In fact, magnetic diffusion renders the study of Alfvén waves very difficult in the lab. The very first experimental hint of Alfvén waves was obtained by Lundquist (1949) in a cylindrical vessel under a uniform magnetic field. He used mercury as a working fluid and a field intensity of 1 T. He excited Alfvén waves by oscillating a crenelated disk at the base of the cylinder, and searched for resonances associated to a standing wave. Lundquist did not reach the resonance peak and pointed out the strong effect of magnetic damping in these experiments. Using liquid sodium, Lehnert (1954a) was able to observe a resonance peak, in agreement with theoretical predictions. Jameson (1964) devised a more elaborate toroidal device and measured a sharp resonance from Alfvén waves excited by current sheets at the walls of the torus. The Alfvén waves excited in these devices were all axisymmetric and toroidal. They were called 'torsional' by Lehnert (1954a), a terminology which is still widely used in the solar corona context (e.g. Spruit 1982). Note that they differ from what we call torsional Alfvén waves: they are not invariant along the symmetry axis, since they propagate in that direction. Applying magnetic fields up to 13 T on a gallium alloy, Alboussiere et al. (2011) were able to document the propagation of Alfvén waves, while previous studies focused on standing wave resonances. Their waves were poloidal instead of toroidal.

One important difference between our experiment and previous ones is that we apply a dipolar

magnetic field instead of a constant homogeneous magnetic field. Note that the propagation of torsional Alfvén waves requires a magnetic field component perpendicular to the axis of rotation.

Global rotation is a required ingredient for torsional Alfvén waves, and was absent from all laboratory experiments so far. In contrast, several theoretical studies have considered the influence of rotation, starting with the pioneer analysis of Lehnert (1954b). Lehnert showed that the influence of rotation depends upon the ratio of the rotation time to the Alfvén time, which is now called the Lehnert number, following Jault (2008). For small enough Lehnert number (strong rotation), he found that two families of waves are present: fast inertial waves modified by the magnetic field, and slow Alfvén waves modified by rotation. One important property of Alfvén waves is that their kinetic and magnetic energies are equal. Lehnert points out that this equipartition is lost in the presence of rotation. More recently, Sreenivasan and Narasimhan (2017) have conducted a thorough analysis of the damping of magnetohydrodynamic waves with rotation focused towards liquid metals. They study the evolution of waves triggered by an initial velocity perturbation, and determine several characteristic times separating different dynamic regimes. The time-evolution of the magnetic and kinetic energies of the two families of waves follow power laws with different exponents in the propagation and diffusion regimes. Both studies consider an infinite domain with a homogeneous magnetic field aligned with the rotation axis. In contrast, Bardsley and Davidson (2016) investigated the case when the magnetic field is perpendicular to the rotation axis. Waves leading to quasi-geostrophy are then observed: they propagate at the Alfvén wave velocity in the direction of the magnetic field, and at the group velocity of inertial waves along the rotation axis, and exhibit energy equipartition.

In the Earth's core, the presence of spherical boundaries has a strong impact: inertial waves build geostrophic columns, which carry most of the energy and allow for the propagation of torsional Alfvén waves in the direction perpendicular to the rotation axis. The relevant parameters for the Earth's core yield low magnetic diffusivity and strong rotation, and this is the regime studied by Jault (2008) and colleagues (Gillet et al. 2012; Schaeffer et al. 2012). Their studies demonstrate that quasi-geostrophic (z-invariant) structures dominate the flows at short time-scales, even when the magnetic field is strong as measured by the Elsasser number (the ratio of Lorentz to Coriolis forces). Indeed, Jault (2008) demonstrates that geostrophic torsional Alfvén waves persist for an Elsasser number of order 10 as long as the Lehnert is smaller than 3×10^{-2}.

The DTS-Ω experiment was built to explore the magnetostrophic regime, with Elsasser number around 1 (Cardin et al. 2002; Nataf et al. 2006; Brito et al. 2011). Here, we trigger waves mechanically

by sudden jerks of its inner sphere, in order to investigate the formation of Alfvén waves and torsional Alfvén waves in a situation where magnetic diffusion plays an important role.

The present paper is organized as follows. In section 2, we present the experimental set-up of DTS-Ω, the first raw observations, the numerical set-up and the governing equations. Section 3 presents the expected ideal Alfvén and torsional Alfvén waves, discusses the effect of magnetic diffusion, and introduces the relevant dimensionless numbers. The main experimental and simulation results are presented in section 4. We examine the role of rotation through the combined analysis of the magnetic waveforms, the electric potentials, and the fluid velocity field measured by Ultrasound Doppler Velocimetry (UDV). Detailed comparison with the numerical simulations permits deciphering the behaviour of Alfvén waves and torsional Alfvén waves in a dipolar magnetic field. Section 5 establishes the scaling laws of the time evolution of the kinetic and magnetic energies. Section 6 summarizes the main conclusions of this work and provides some perspectives.

2 EXPERIMENTAL AND NUMERICAL SET-UP

We first recall the DTS-Ω experimental set-up and present the first raw observations of torsional wave signals. We then detail the numerical set-up and the equations we solve.

2.1 Experimental set-up

The DTS experiment produces a rotating spherical Couette flow in a dipolar magnetic field. It displays all required ingredients to trigger and observe torsional Alfvén waves. Its recently upgraded version DTS-Ω includes an embarked electronics, which permits the simultaneous acquisition of 200 signals in the rotating frame. Figure 1a shows the DTS-Ω set-up with its stainless steel outer shell (radius $r_o = 210$ mm) containing 50 liters of liquid sodium, a good electric conductor. Its inner sphere (radius $r_i = 74$ mm) consists in a copper shell housing a strong permanent magnet, which provides a nearly dipolar magnetic field with a vertical axis. See Brito et al. (2011) for more details.

The inner sphere and the outer shell spin independently around the vertical axis at rotation rates f_i and f_o respectively. For this study, we spun DTS-Ω up to $f_o = 15$ Hz. Once in solid body rotation ($f_o = f_i \equiv f$), we trigger Alfvén waves by sudden jerks of the inner sphere. We define the angle $\Delta\varphi$ swept by the inner sphere during the jerk time t_{jerk}. We characterize the jerk by its magnetic Reynolds number $Rm_{jerk} = r_o U_{jerk}/\eta$, with $U_{jerk} = r_i \Delta\varphi / t_{jerk}$, and η the magnetic diffusivity.

In the DTS-Ω experiment, the magnetic field is produced by a permanent magnet enclosed in the inner sphere. The field is mainly axisymmetric and dipolar along a vertical axis in the fluid. In

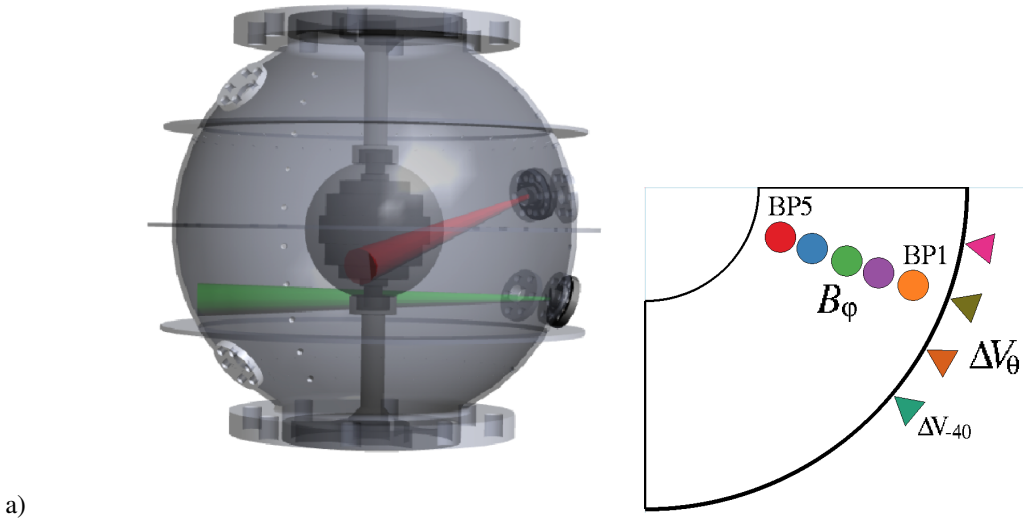

a) b)

Figure 1. Sketch of the DTS-Ω set-up. (a) The spherical shell of DTS-Ω showing the inner sphere and its shaft viewed through the 5mm-thick stainless steel outer shell. Little holes on the outer shell host electrodes. Ultrasound beams used for Doppler velocimetry are shot from two ports. A sleeve (not shown) penetrating radially from a port hosts Hall magnetometers. (b) sketch of the positions of the B_φ magnetometers in the sleeve, and of the ΔV_θ electric potential measurements at the surface, in a meridional section of the DTS-Ω experiment (lower quadrant).

spherical coordinates (r, θ, φ), we get:

$$\mathbf{B_d}(r,\theta) = \frac{\mu_0 \mathcal{M}}{4\pi r^3}(2\hat{\mathbf{r}}\cos\theta + \hat{\theta}\sin\theta), \tag{1}$$

with $\mathcal{M} \simeq 700$ Am^2, where $\hat{\mathbf{r}}$ and $\hat{\theta}$ are the unit vectors in the radial and orthoradial directions, respectively. The intensity of the imposed field reaches 345 mT at the pole of the inner sphere $(r = r_i, \theta = 0)$, decreasing to 7.5 mT at the equator of the outer sphere $(r = r_o, \theta = \pi/2)$. We use this latter value to define our magnetic intensity scale B_0. Table 1 recalls these values and lists the kinematic viscosity ν, the magnetic diffusivity η, and the magnetic Prandtl number $Pm = \nu/\eta$ of liquid sodium.

In this article, we present signals of the azimuthal magnetic field B_φ measured in a sleeve installed in one of the two -20°-latitude ports, visible in Figure 1a. We have also recorded additional signals at

[h]

r_i	r_o	$B_d(r_i, \pi/2)$	$B_d(r_o, \pi/2)$	η	ν	Pm
mm	mm	mT	mT	m^2/s	m^2/s	ν/η
74	210	175	7.5	8.8×10^{-2}	6.5×10^{-7}	7.4×10^{-6}

Table 1. Main relevant properties of the sodium-filled DTS-Ω experiment.

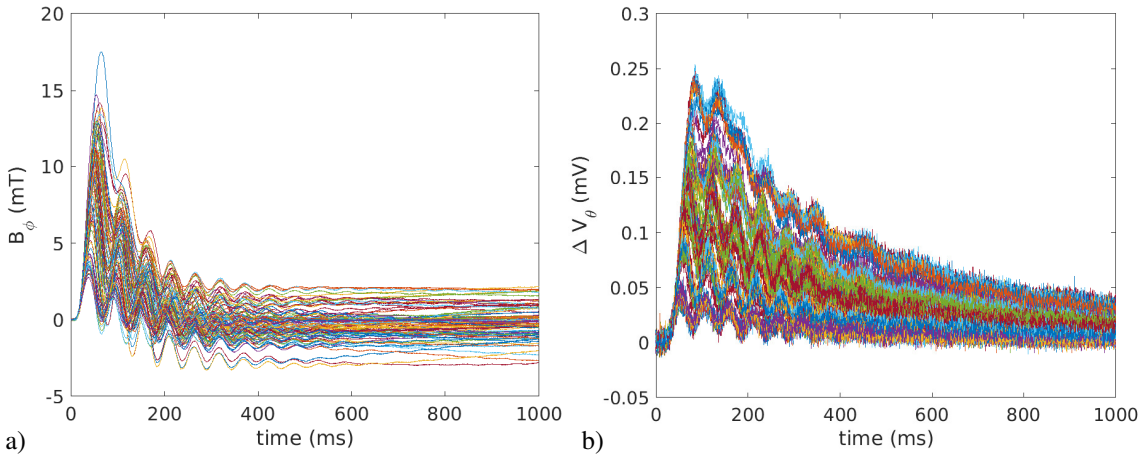

Figure 2. (a) Magnetic (BP5) and (b) electric (ΔV_{-40}) signature of 99 different jerks of the inner sphere. The rise time t_{rise} of these jerks range from 16 to 56 ms, and the angle $\Delta\varphi$ swept by the inner sphere during a jerk ranges from 16° to 190°.

10° and 40°. Electric potential differences ΔV_θ are measured along a meridian between electrodes 10°-apart, implanted in the outer stainless steel shell (see Figure 1a). The position of these measurements is shown in Figure 1b.

Let's have a look at the typical B_φ and ΔV_θ signals we obtain.

2.2 Raw observations

Figure 2 displays the signals recorded for a collection of 99 jerks of the inner sphere, during 1 second after the jerk start. The rotation rate is $f = 15$ Hz. The B_φ magnetic signal closest to the inner sphere ($r_{\text{BP5}} = 94$ mm) at a latitude of -20° (see Figure 1b) is shown in Figure 2a. Its maximum amplitude ranges from 3 to 18 mT. Figure 2b is the corresponding electric potential difference ΔV_{-40} at the surface between latitudes -45° and -35°. Its maximum amplitude ranges from 0.04 to 0.24 mV.

In both cases, the dispersion of the curves at $t = 0$ gives an indication of the precision of the measurements. While the electric signals tend to zero at long times, the B_φ signals level off at various values. This is due to non-axisymmetric components of the magnetic field produced by the magnet inside the inner sphere (see Appendix A1.1). We also note strong oscillations at a frequency of about 18 Hz. These are due to rapid oscillations of the inner sphere triggered by the jerk (see Appendix B). We will deal with these experimental artefacts later on.

In order to decipher the behaviour of torsional Alfvén waves, we ran numerical simulations, which we now describe.

[h]

shell material	radial extent mm	electric conductivity $10^6\ \Omega^{-1}\mathrm{m}^{-1}$
stainless steel	$210 : 215$	1
liquid sodium	$74 : 210$	9
copper	$\sim 63 : 74$	38

Table 2. Electric conductivity shells in the sodium-filled DTS-Ω experiment.

2.3 Numerical set-up

We have performed pseudo-spectral numerical simulations of the generation and propagation of torsional Alfvén waves in a spherical fluid shell without and with global rotation using the XSHELLS v1.4 software (Figueroa et al. 2013). XSHELLS simulates MHD incompressible fluids and time-steps both induction and Navier-Stokes equations (presented in section 2.4) in the spherical configuration. The code uses second order finite differences in the radial direction with many points concentrated near the walls (boundary layers) and the spherical harmonic transform library SHTns (Schaeffer 2013) in the latitudinal direction, as well as hybrid parallel execution using OpenMP and/or MPI. XSHELLS v1.4 uses a semi-implicit time-stepping scheme with diffusive terms treated by the Crank-Nicolson method and all other terms (including non-linear terms) are treated by a second-order Adams-Bashforth scheme. XSHELLS has been used previously to efficiently simulate the DTS experiment (Figueroa et al. 2013; Cabanes et al. 2014a), the DTS-Ω experiment (Kaplan et al. 2018), as well as unmagnetized spherical Couette (Barik et al. 2018) and torsional Alfvén waves (Gillet et al. 2012; Schaeffer et al. 2012; Schaeffer and Jault 2016).

We model torsional Alfvén waves with an imposed dipolar magnetic field, keeping parameters as close as possible to those of the DTS-Ω experiments. Note that XSHELLS simulations do not include geometric details of the experiment such as the shaft holding the inner sphere. We only consider axisymmetric (m=0) solutions. All physical properties are the same as in the experiment, except for the viscosity, which cannot be as low as in the experiment for numerical reasons. Nevertheless, all simulations are in the low magnetic Prandtl number regime, with $Pm \leq 10^{-3}$. The actual simulation parameters are summarized in Table A2 of Appendix D.

No-slip boundary conditions are used for the fluid velocity field on the inner and outer surfaces. The magnetic boundary conditions require a special treatment because of the electric conductivity jumps between the inner sphere, the liquid, and the outer shell, which we keep the same as in the DTS-Ω experiment, given in Table 2. The procedure is described in detail in Appendix C of Cabanes et al. (2014a).

We have introduced two types of jerk time-function, the first one is a boxcar, and the second one closely mimics the actual jerk time-function of the experiment (see Appendix A2). The angle swept by the inner sphere during a jerk typically reaches 90° or more in the experiment, yielding Rm_{jerk} values of order unity, implying Reynolds numbers $Re_{jerk} = Rm_{jerk}/Pm$ larger than 10^5. Even though we use larger Pm values in the numerical simulations, we are still in a non-linear regime. A group of simulations considers smaller jerk-angles corresponding to quasi-linear regimes.

2.4 Equations

The dynamical behaviour of the fluid motion and magnetic induction are described by the Navier-Stokes equations (2, 3) and the induction equations (4, 5),

$$\underbrace{\frac{\partial \mathbf{u}}{\partial t}}_{F_{dt}} + \underbrace{(\mathbf{u}\cdot\nabla)\mathbf{u}}_{F_{adv}} + \underbrace{2\mathbf{\Omega}\times\mathbf{u}}_{F_{Cor}} \tag{2}$$

$$= \underbrace{-\frac{1}{\rho}\nabla P}_{F_P} + \underbrace{\frac{1}{\rho\mu_0}(\nabla\times\mathbf{b})\times\mathbf{B_d}}_{F^{lin}_{Lor}} + \underbrace{\frac{1}{\rho\mu_0}(\nabla\times\mathbf{b})\times\mathbf{b}}_{F^{NL}_{Lor}} + \underbrace{\nu\nabla^2\mathbf{u}}_{F_{diff}}$$

$$\nabla\cdot\mathbf{u} = 0 \tag{3}$$

$$\underbrace{\frac{\partial \mathbf{b}}{\partial t}}_{G_{dt}} = \underbrace{\nabla\times(\mathbf{u}\times\mathbf{B_d})}_{G^{lin}_{ind}} + \underbrace{\nabla\times(\mathbf{u}\times\mathbf{b})}_{G^{NL}_{ind}} + \underbrace{\eta\nabla^2\mathbf{b}}_{G_{diff}} \tag{4}$$

$$\nabla\cdot\mathbf{b} = 0 \tag{5}$$

where $\mathbf{u}$ and $\mathbf{b}$ are the fluid velocity and magnetic fields of the perturbation, respectively, and ρ, ν and η are the density, viscosity and magnetic diffusivity of the fluid. The magnetic diffusivity is defined by $\eta = 1/\sigma\mu_0$ where σ and μ_0 are the electrical conductivity and the magnetic permeability of the fluid.

We choose the outer shell radius r_o as a typical length scale, and the magnetic diffusion time $t_\eta = r_o^2/\eta$ for time scale. As mentioned in section 2.1, the jerk magnetic Reynolds number Rm_{jerk} is of order unity in the experiments and simulations. Therefore we expect $|\mathbf{b}| \ll |\mathbf{B_d}|$, implying that F^{NL}_{Lor} and G^{NL}_{ind} are not dominant compared to respectively F^{lin}_{Lor} and G^{lin}_{ind}. The kinetic Reynolds number Re_{jerk} is large implying that the viscous term F_{diff} is always small at large scale. In the absence of rotation, the inertial term F_{adv} cannot be neglected. With rotation, this term can be compared with the Coriolis term F_{Cor}, using the Rossby number $Ro = U_{jerk}/(2\pi f r_o) \sim 0.1$ for $f = 15$ Hz. Thus, at large scales the non linear term F_{adv} is expected to be non significant compared to the linear term F_{Cor} or F^{lin}_{Lor}. Therefore in the experimental conditions the fluid acceleration F_{dt} is, at large scales, mainly due to the Coriolis force F_{Cor} and the Lorentz force F^{lin}_{Lor}, leading to (6). The induction derivative G_{dt} is mainly due to the electromotive force G^{lin}_{ind} and the dissipation G_{diff}, leading to (7). We note that the pressure P plays a passive role, as it can be removed taking the curl of (6).

$$\underbrace{\frac{\partial \mathbf{u}}{\partial t}}_{F_{dt}} + \underbrace{2\boldsymbol{\Omega} \times \mathbf{u}}_{F_{Cor}} = \underbrace{-\frac{1}{\rho}\nabla P}_{F_P} + \underbrace{\frac{1}{\rho\mu_0}(\nabla \times \mathbf{b}) \times \mathbf{B_d}}_{F_{Lor}^{lin}} \quad (6)$$

$$\underbrace{\frac{\partial \mathbf{b}}{\partial t}}_{G_{dt}} = \underbrace{\nabla \times (\mathbf{u} \times \mathbf{B_d})}_{G_{ind}^{lin}} + \underbrace{\eta \nabla^2 \mathbf{b}}_{G_{diff}} \quad (7)$$

Ideal waves result from (6) and (7) without the ohmic dissipation G_{diff}. The generation of Alfvén waves versus torsional Alfvén waves depends on whether in (6) the Coriolis acceleration F_{Cor} can be neglected or not compared to the Lorentz acceleration F_{Lor}^{lin} (section 3.1). In the non ideal case when Ohmic dissipation G_{diff} cannot be neglected, two characteristic time scales can be defined, a magnetic diffusion time t_η and a Joule time t_J, derived from (7) by comparing G_{diff} to respectively G_{dt} and G_{ind}^{lin} (section 3.2).

3 Alfvén WAVES VERSUS TORSIONAL Alfvén WAVES

3.1 Ideal waves

3.1.1 Ideal Alfvén waves

Ideal (*i.e.,* non-dissipative) Alfvén waves are non-dispersive waves that follow magnetic field lines in a fluid or plasma. The corresponding dispersion relation can be derived from (6) and (7) with $\Omega = 0$ and neglecting the magnetic dissipation term G_{diff}. The local velocity of Alfvén waves $\mathbf{V_A}(\mathbf{r})$ is given by:

$$\mathbf{V_A}(\mathbf{r}) = \frac{\mathbf{B_d}(\mathbf{r})}{\sqrt{\mu_0 \rho}}, \quad (8)$$

where $\mathbf{B_d}(\mathbf{r})$ is the magnetic field at position $\mathbf{r}$ defined in (1). In this case we also have $|\mathbf{u}|/|\mathbf{b}| \approx 1/\sqrt{\mu_0\rho}$ and the characteristic time scale of Alfvén waves is given by $t_A(\mathbf{r}) = r_o\sqrt{\mu_0\rho}/|\mathbf{B_d}(\mathbf{r})|$ (see Table 3).

The travel time of ideal Alfvén waves is determined by integrating $d\ell/V_A(r,\theta)$ along field lines from the source (the surface of the inner sphere, $r = r_i$) to all (r,θ) points. The resulting wavefronts are shown in Figure 3a. Ideal Alfvén waves reach the outer sphere in only 120 ms (at the pole) to 420 ms (at the equator). Note that we have only drawn wavefronts emitted from the upper hemisphere, and do not consider reflexions at the boundaries. Following the dipolar field lines, some waves cross the equator and reach the opposite side of the inner sphere. We will see a consequence of this behaviour in section 4.2.

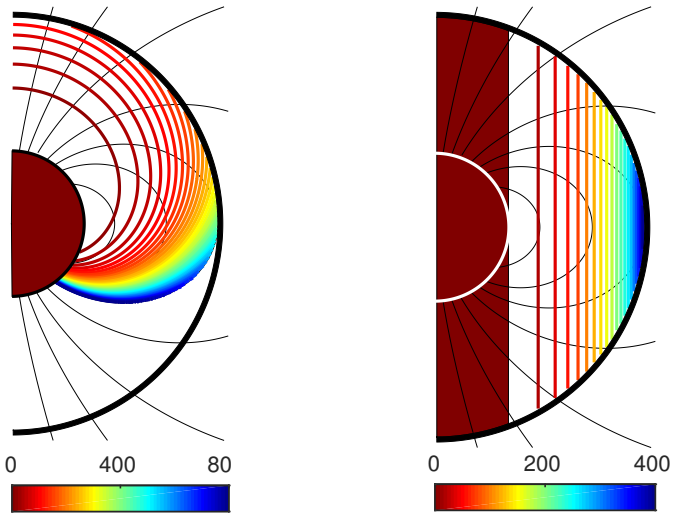

a) b)

Figure 3. Wavefronts of (a) ideal Alfvén waves and (b) ideal torsional Alfvén waves in a dipolar magnetic field. The waves are triggered by a jerk of the inner sphere (in brown). The color scales give the travel times in milliseconds for the DTS-Ω parameters.

3.1.2 Ideal torsional Alfvén waves

In a rapidly rotating sphere, such that F_{Cor} cannot be neglected in (6), the Coriolis force inhibits velocity variations along the rotation axis $\hat{\mathbf{z}}$. Torsional Alfvén waves are geostrophic and propagate along the cylindrical radius direction $s = r\sin\theta$, with a velocity given by:

$$\mathbf{V_{TA}}(s) = \hat{\mathbf{s}}\sqrt{\frac{1}{2h(s)\mu_0\rho}\int_{-h}^{h} B_s^2(s,z)dz}, \tag{9}$$

with $h(s) = \sqrt{r_o^2 - s^2}$ being half the height of the geostrophic cylinder at s (e.g. Gillet et al. 2010; Jault and Finlay 2015). We only consider torsional Alfvén waves propagating outside the cylinder tangent to the inner sphere, which represents the source of the wave, and we do not consider reflexions at the boundaries. We obtain the travel time of torsional Alfvén waves by integrating $ds/V_{TA}(s)$ from that source ($s = r_i$) to all $s > r_i$. The resulting wavefronts are shown in Figure 3b. Ideal torsional Alfvén waves reach the equatorial region of the outer sphere in about 420 ms.

3.1.3 The Lehnert number

Torsional Alfvén waves appear provided that the Coriolis force is sufficiently strong compared to the Lorentz force, which corresponds in (6) to strong enough F_{Cor} compared to F_{Lor}^{lin}. Introducing a

	t_η	t_A	t_J	Lu	Le	Λ	E_η	Rm_{jerk}	Re_{jerk}
	$\frac{r_o^2}{\eta}$	$\frac{r_o\sqrt{\mu_0\rho}}{B_d(r)}$	t_A^2/t_η	$\frac{r_o B_d(r)}{\eta\sqrt{\mu_0\rho}}$	$\frac{B_d(r)}{2\pi f r_o\sqrt{\mu_0\rho}}$	Lu Le	Le/Lu	$\frac{U_{jerk}\, r_o}{\eta}$	Rm_{jerk}/Pm
$B_d(r_i,\pi/2)$	500	41	3.4	12	0.26	3.15	0.021	5.52	751,000
$B_d(r_o,\pi/2)$	500	960	1,840	0.53	0.011	0.0058	0.021	5.52	751,000

Table 3. Magnetic diffusion time, Alfvén time, Joule time (all in milliseconds) and key dimensionless numbers for torsional Alfvén waves in the DTS-Ω experiment, calculated taking either $B_d(r_i,\pi/2)$ or $B_d(r_o,\pi/2)\equiv B_0$ as the intensity of the imposed magnetic field. The rotation rate is $f=15$ Hz, and the jerk sweeps an angle $\Delta\varphi=180^\circ$, over a time $t_{\rm jerk}=100$ ms ($t_{rise}=50$ ms).

typical rotation time $t_\Omega=\Omega^{-1}$ such condition corresponds to $t_\Omega \ll t_A$. Lehnert (1954b) was the first to study the effect of the Coriolis force on Alfvén waves. Following Jault (2008), we define the Lehnert number as:

$$Le=\frac{t_\Omega}{t_A}=\frac{B_d(r)}{\Omega r_o\sqrt{\mu_0\rho}} \tag{10}$$

Jault (2008) showed that clearly z-invariant torsional Alfvén waves form when the Lehnert number is smaller than about 3×10^{-2}. As shown in Table 3, we reach values of the Lehnert number between 1.1×10^{-2} and 2.6×10^{-1} in our experiment at our highest rotation rate $f=\Omega/2\pi=15$ Hz, depending on whether we pick for $B_d(r)$ the intensity of the equatorial magnetic field at $r=r_o$ or $r=r_i$.

3.2 The effect of magnetic diffusion

While dissipation can often be neglected in natural systems such as planetary cores and stars, it plays a major role in laboratory experiments.

3.2.1 The Lundquist number

One can measure the role of magnetic diffusion by comparing the Alfvén time t_A to the magnetic diffusion time t_η. This yields the Lundquist number:

$$Lu=\frac{t_\eta}{t_A}=\frac{r_o B_d(r)}{\eta\sqrt{\mu_0\rho}}. \tag{11}$$

Table 3 shows that in our experiment the Lundquist number decreases from a value of 12 at $r=r_i$ to 0.53 at $r=r_o$. Therefore, we expect an important magnetic dissipation.

3.2.2 The Joule damping time

The *quasistatic* approximation is widely used in studies of MHD flows in liquid metals (e.g. Roberts 1967; Sommeria and Moreau 1982; Siso-Nadal and Davidson 2004). It is a high magnetic diffusion

limit, which assumes that G_{dt} is negligible in (7). For a large imposed magnetic field, the fluid acceleration F_{dt} is dominated by the Lorentz force F_{Lor}^{lin} in (6). This yields a characteristic time $t_J = \rho/(\sigma B_d^2(r))$, which is called the Joule damping time. The values of t_J are listed in Table 3 for the DTS-Ω set-up.

It only amounts to $t_J = 3.4$ ms when we pick $B_d(r_i)$ as the relevant magnetic field intensity. One might therefore infer that Joule damping controls the flow dynamics near the inner sphere. This is not the case. Indeed, the Joule damping time can be written as $t_J = t_A/Lu$, showing that it will always be small at large Lundquist numbers, which is in contradiction with the fact that magnetic diffusion is *small* at large Lu. Physically, what happens is that the presence of the G_{dt} term reduces the electric currents $\mathbf{j}$ needed to produce $\mathbf{b}$, making the induction term G_{ind}^{lin} much smaller than assumed for deriving t_J. The quasistatic approximation cannot be used when dealing with Alfvén waves.

4 EXPERIMENTAL AND SIMULATED SIGNALS: THE EFFECT OF ROTATION

4.1 Early signals

Let's first consider signals arriving within 80 ms from the jerk start. The large range of the raw signals illustrated by Figure 2 is due to the variety of the inner sphere jerks we produced. Indeed, we cannot control precisely the duration and amplitude of the jerks we trigger. We characterize the jerks by the total angle $\Delta\varphi$ they swept, and their rise time t_{rise}, as described in Appendix A. Here, we select 29 jerks of similar size ($\Delta\varphi = 110^\circ \pm 20^\circ$), with a rise time between 35 and 46 ms, and we stack the corresponding records. Figure 4a shows the resulting B_φ signals at latitude -20° at all five radial positions displayed in Figure 1b. We see a clear time progression of the signals, in excellent agreement with the simulation with $\Delta\varphi = \pi/2$ and $t_{rise} = 40$ ms shown in Figure 4c. Only $\simeq 16$ ms separate the BP5-signal from the BP1-signal (measured at mid-height) in the experiment, compared to 20 ms ($= 0.04\, t_\eta$) in the simulation, while an ideal torsional Alfvén wave would have taken 160 ms. This illustrates the key role of magnetic diffusion in the experiment. Figure 4b shows the electric potential differences at the surface of the sphere at the four latitudes displayed in Figure 1b. They compare very well with their simulation counterparts shown in Figure 4d. In both cases, the signals have the same shape at all four latitudes, and superpose almost exactly with the BP1 magnetic signal.

We note that all experimental signals arrive $t_{lag} \simeq 10$ ms $= 0.02\, t_\eta$ late compared to the simulations. This is due to a short delay between the initiation of the jerk on the inner sphere pulley and the reaction of the inner sphere itself. Indeed, the inner sphere of DTS-Ω is entrained via a magnetic coupler, as described in Brito et al. (2011). In Appendix B, we use t_{lag} to compute the angle lag $\delta\varphi_{lag}$

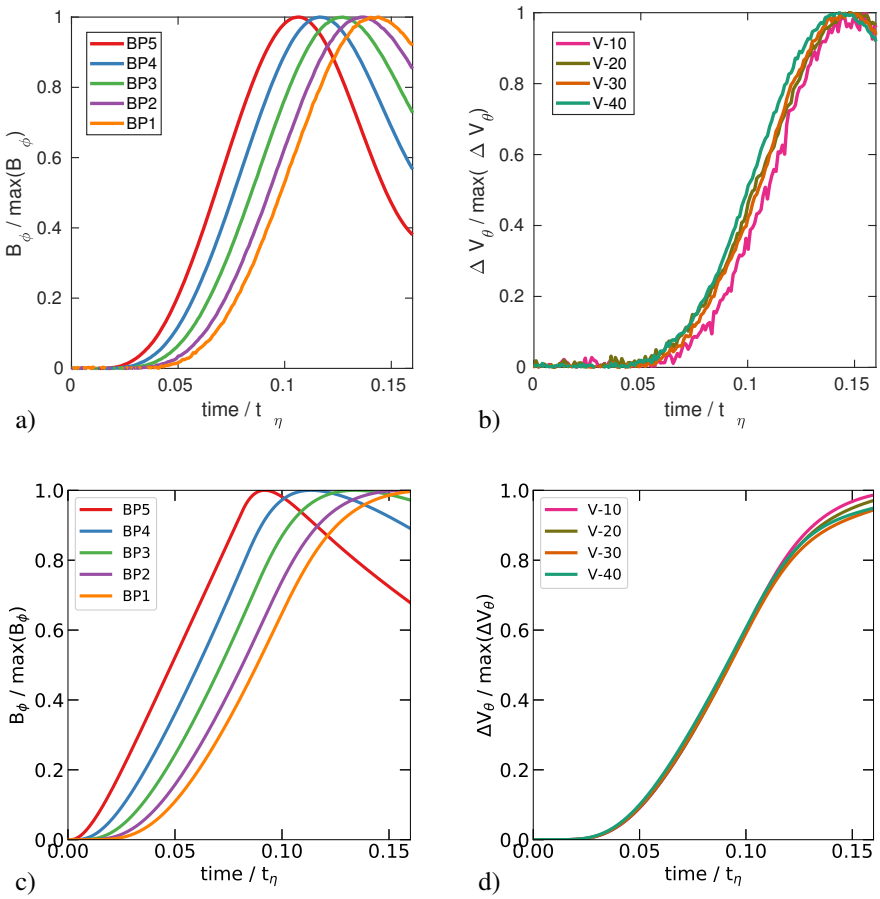

Figure 4. Magnetic and electric waveforms of torsional Alfvén waves in the DTS-Ω experiment for a rotation rate $f = 15$ Hz. Observed (a) and simulated (c) B_φ azimuthal magnetic signals inside the liquid at a latitude of -20° for five radii color-coded as in Figure 1b. Observed (b) and simulated (d) ΔV_θ electric potential differences at the surface of the stainless steel outer shell at four latitudes. All signals are normalized to their maximum amplitude, and plotted versus time normalized by the magnetic diffusion time t_η.

of the inner sphere with respect to its pulley by integrating the instantaneous rotation rate of the pulley during the constant acceleration rise, and get: $\delta\varphi_{lag} \simeq 1.2°$.

We now examine the complete waveforms over two magnetic diffusion times, and compare the rotating case ($f = 15$ Hz) with the non-rotating one ($f = 0$). We select stronger jerks than in the previous section, in order to minimize the contribution of the inner sphere oscillations to the signals.

4.2 Magnetic waveforms

Figure 5a shows the B_φ stacks of a selection of 18 jerks of similar size ($\Delta\varphi = 155° \pm 25°$), with a rise time between 50 and 56 ms, for $f = 0$. By stacking the signals, we get rid of the offsets that were visible after the jerks in Figure 2a. They only show up in the root mean square fluctuations (shaded

area) around the mean. In contrast with Figure 4, we retain the amplitudes of the different signals, and we clearly see the strong attenuation of the magnetic field (from BP5 to BP1) as the wave moves away from the inner sphere.

Figure 5b shows B_φ stacks for a similar selection of 22 jerks at $f = 15$ Hz. The differences with Figure 5a are subtle, but we note slightly larger amplitudes, a wider positive pulse, and almost no negative overshoot. These differences are also met in the corresponding simulations ($\Delta\varphi = \pi$ and $t_{rise} = 50$ ms) shown in Figures 5c and 5d, which use the same jerk time-function as the experiments (see Appendix A2).

The negative overshoot of B_φ near the inner sphere is somewhat unexpected. The numerical simulations help us get a better understanding when we examine the isolines of the azimuthal magnetic field in a meridional plane. Figures 6a and 6b show such snapshots at $t = 0.3\, t_\eta$ for $f = 0$ and $f = 15$ Hz, respectively, while Figures 6c and 6d show the corresponding U_φ isolines. The sudden positive jerk ($U_\varphi > 0$, red in Figure 6c) entrains the feet of the field lines of the imposed dipole on the inner sphere, producing a negative (green) B_φ in the upper hemisphere and positive (violet) B_φ in the lower hemisphere.

However, a patch of reversed B_φ polarities shows up clearly near the equator of the inner sphere. This is the signature of an Alfvén wave that originated in the opposite hemisphere (see Figure 3a): it retains its original polarity throughout. Diffusion strongly smears both the magnetic and the velocity signals, and we can better see this phenomenon if we reduce the diffusion by two orders of magnitude, as in the simulations displayed in Figure 7. In the latter, we also see the signature of Alfvén waves reflected on the inner sphere. Reflection of an Alfvén wave on a rigid conducting wall (our copper inner sphere) reverses the polarity of velocity while the magnetic perturbation retains its polarity (Alfvén and Fälthammar 1963, p.86).

Torsional Alfvén waves do not travel from one hemisphere to the other (see Figure 3b); hence the absence of B_φ negative overshoot.

We note that the differences between the rotating and non-rotating cases are subtle for the magnetic field (Figures 5ab and 6ab), while the velocity fields appear clearly different in Figure 6cd. The flow is dominated by an equatorial ring for $f = 0$, while it rapidly takes the shape of geostrophic cylinders for $f = 15$ Hz.

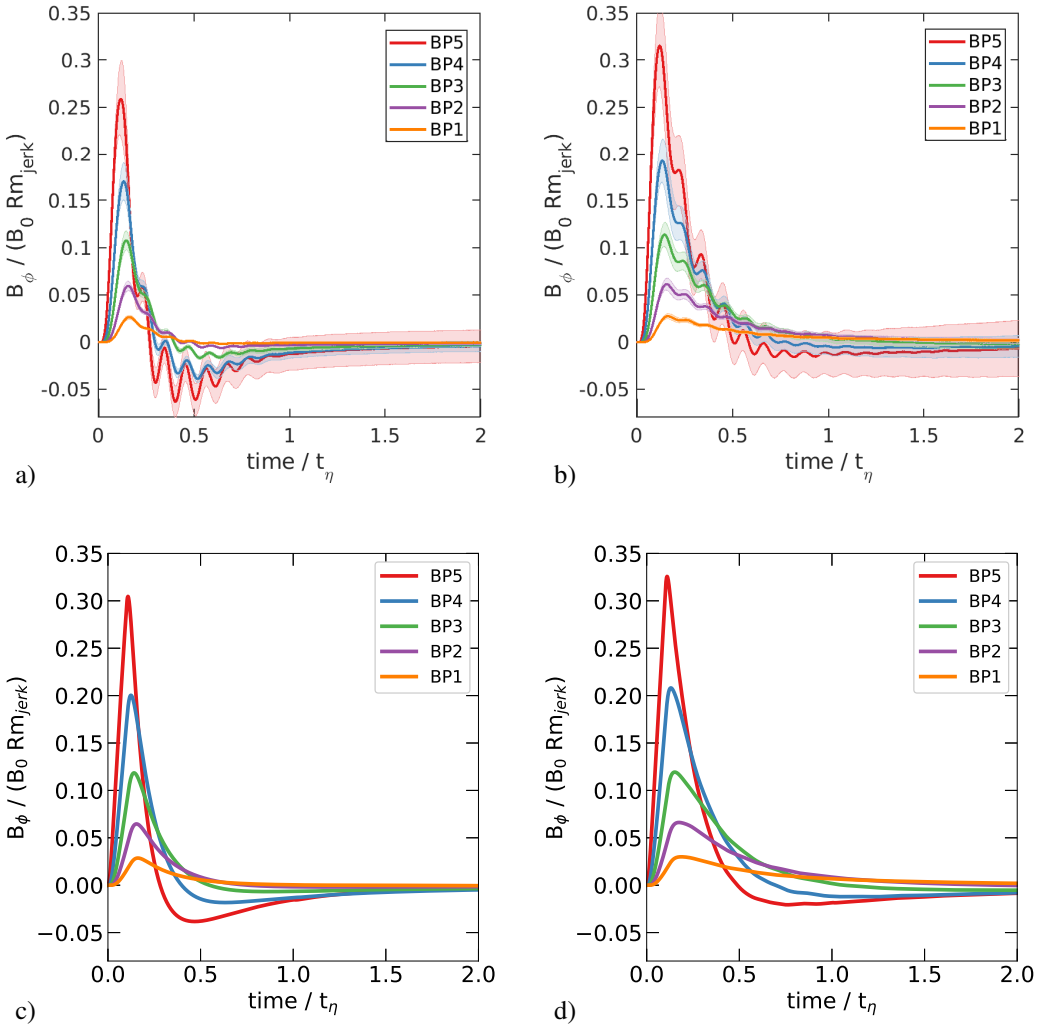

Figure 5. Azimuthal magnetic field B_φ of the wave as a function of time at a latitude of $-20°$ at 5 radii color-coded as in Figure 1b. Time is given in magnetic diffusion time t_η units. Magnetic field is normalized by $B_0\, Rm_{jerk}$. (a) stack of B_φ for 18 similar jerks with no rotation ($f = 0$). The shaded region represents the *rms* around the mean. (b) stack of B_φ for 22 similar jerks with rotation ($f = 15$ Hz). (c) numerical simulation for $f = 0$. (d) numerical simulation for $f = 15$ Hz.

4.3 Electric potentials

Within some limits, surface electric potentials can serve as a proxy of the fluid velocity (Lehnert 1954a). From Ohm's law, following Brito et al. (2011), we can write:

$$U_\varphi = \frac{1}{B_r}\frac{\Delta V_\theta}{r_o \Delta\theta}, \tag{12}$$

where U_φ represents some fluid azimuthal velocity in the bulk, B_r is the radial component of the imposed dipole at colatitude θ, and ΔV_θ is the finite electric potential difference between points at latitude $\theta + \Delta\theta/2$ and $\theta - \Delta\theta/2$.

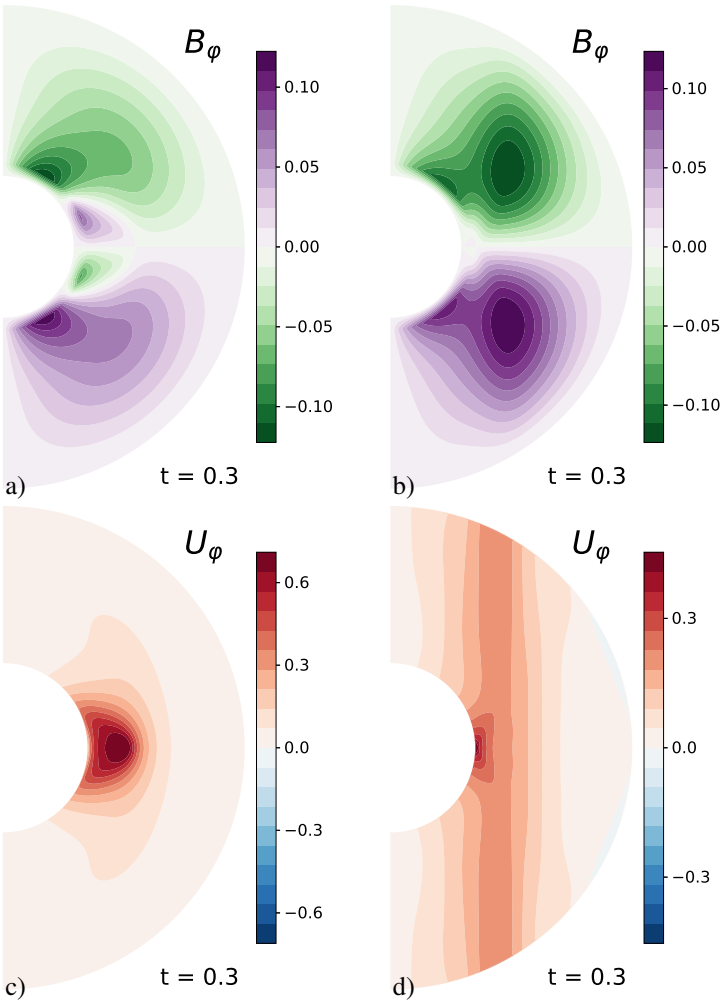

Figure 6. Comparison of meridional snapshots of computed Alfvén waves (left; $f = 0$) versus computed torsional Alfvén waves (right; $f = 15$ Hz) for the B_φ azimuthal magnetic field (a,b), and U_φ azimuthal velocity field (c,d) at time $t = 0.3\,t_\eta$. Magnetic field B_φ is normalized by $B_0\,Rm_{jerk}$. Azimuthal fluid velocity U_φ is normalized by $U_{jerk} = r_i \Delta\varphi / t_{jerk}$.

Figures 8a and 8b display the waveforms of the surface electric potential differences ΔV_θ at latitudes from $-10°$ to $-40°$, for $f = 0$ and $f = 15$ Hz, respectively. The selection of jerks is the same as for Figure 5.

The maximum amplitude increases with latitude, a consequence of the increase of B_r in equation 12. We note that for $f = 15$ Hz the amplitudes of the electric potentials decay much more slowly than that of the magnetic signals.

Figures 8c and 8d show the corresponding synthetic electric potential differences computed in our simulations. We recover the same behaviour as in the experiments, except that the simulated signals last longer than we observe for $f = 0$. Note the much broader initial pulse for $f = 15$ Hz in both the experiments and the simulations. Surprisingly, the simulated electric potentials show some wiggles for

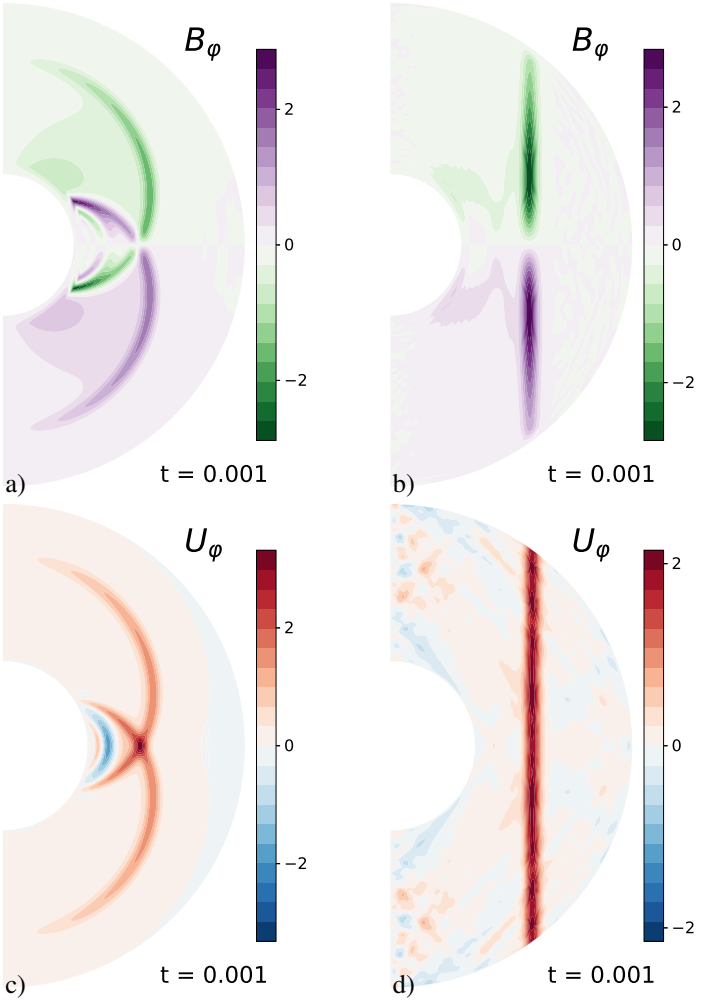

Figure 7. Meridional snapshots of Alfvén waves for simulations with a Lundquist number 100 times larger than in DTS-Ω. (a,c) without rotation at time $t = 0.001\, t_\eta$. (b,d) with rotation rate $f = 15$ Hz at time $t = 0.001\, t_\eta$. U_φ and $B_\varphi/\sqrt{\rho\mu_0}$ both in units of r_o/t_η. See parameters for these simulations in Table A2.

$f = 15$ Hz. In fact, these are the signature of inertial modes, which are excited by the jerk. There is a hint of their presence in the observed signals as well, somewhat obscured by the presence of inner sphere oscillations (see Appendix B).

Note that the amplitudes of the simulated waveforms for both B_φ and ΔV_θ match fairly well those of the experiments. For that, we had to reduce the electric conductivity of the inner sphere shell from that of copper down to that of liquid sodium. This accounts for electric coupling issues as discussed in Appendix C. Similarly, the electric potentials in the upper hemisphere (not shown) are somewhat weaker than in the lower one when $f = 0$.

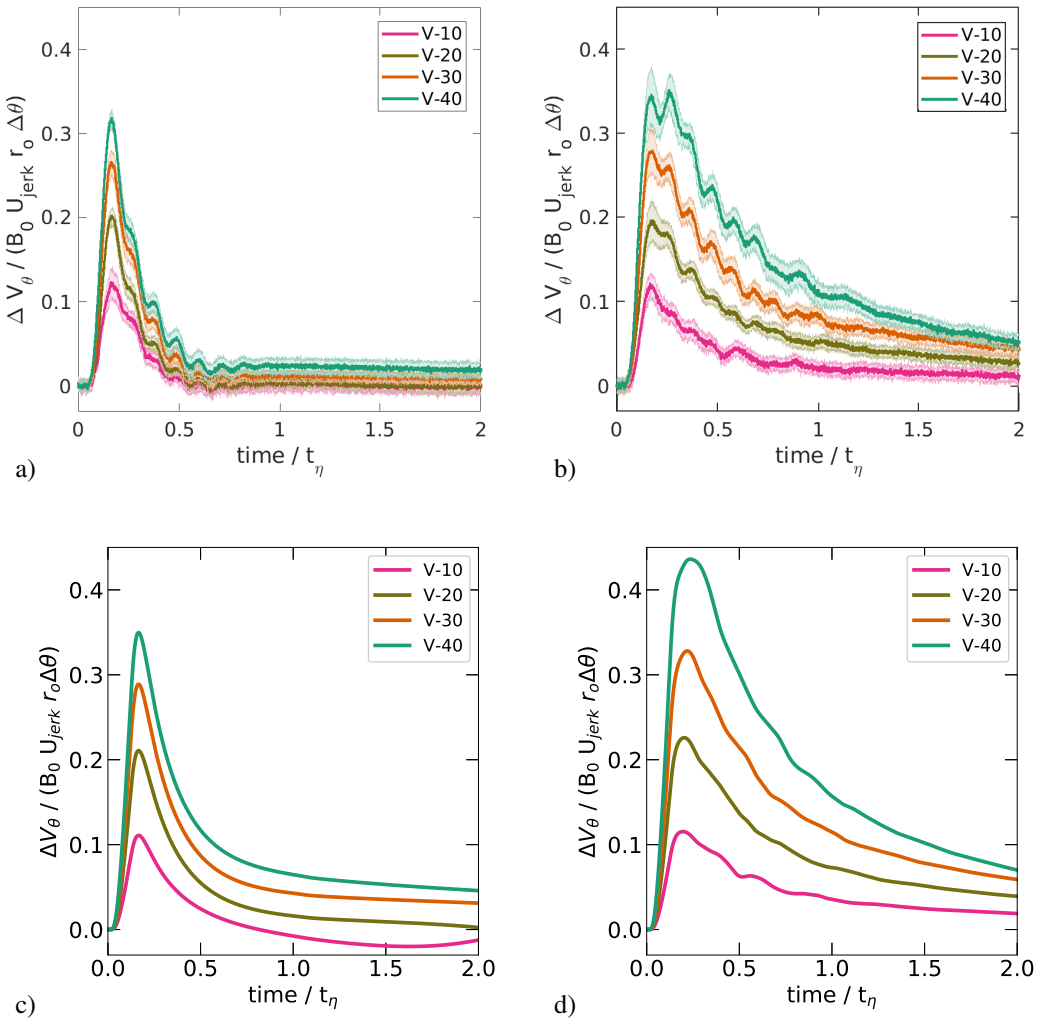

Figure 8. Orthoradial electric potential differences ΔV_θ as a function of time at the surface of the outer sphere, at 4 latitudes color-coded as in Figure 1b. Time is given in magnetic diffusion time t_η units. Electric potential difference is normalized by $B_0\, U_{jerk}\, r_o\, \Delta\theta$, where $\Delta\theta = 10°$ is the latitudinal distance between the two electrodes. (a) stack of ΔV_θ for 18 similar jerks with no rotation ($f = 0$). The shaded region represents the *rms* around the mean. (b) stack of ΔV_θ for 22 similar jerks with rotation ($f = 15$ Hz). (c) numerical simulation for $f = 0$. (d) numerical simulation for $f = 15$ Hz.

4.4 Time evolution of the magnetic and velocity fields

The numerical simulations enable us to better understand the combined time evolution of the magnetic and velocity fields. Going back to Figure 6, we can first stress the differences between the case without rotation (Figure 6ac) versus the case with rotation (Figure 6bd). The main difference is the organization of the velocity field in geostrophic cylinders around the inner sphere in the presence of rotation. This characteristic signature of torsional Alfvén waves appears to be present in the experimental conditions, despite the important magnetic diffusion.

In the case without rotation, we note that the maximum of the U_φ velocity occurs in the equatorial plane and propagates outwards, while no magnetic field line points in that direction. The radial velocity is also strong there. As the Alfvén wave velocity blob propagates away from the inner sphere, it experiences a smaller magnetic field, and inertia takes over. The tip of the resulting equatorial sheet progressively evolves into a typical mushroom shape, as shown in movies Up-0.mp4 and Bp-0.mp4 (see supplementary material). Although Alfvén waves are linear by definition, we observe a clear nonlinear behaviour in this simulation. This is not surprising given the large value of the hydrodynamic Reynolds number $Re \sim 10^5$ in this simulation (and even larger in the corresponding experiment $Re \sim 2 \times 10^6$).

In the rotating case, we observe that jerks of the inner sphere trigger inertial waves. Some of them end up building the geostrophic cylinder that carries the torsional wave. Others reflect on the outer shell and form oscillating inertial modes, which modulate the velocity field (Figure 6d) and the surface electric potentials (Figure 8bd). This is best seen in the movies Up-15.mp4 and Bp-15.mp4 (see supplementary material). The shorter the jerk duration t_{jerk}, the stronger the inertial modes.

4.5 Velocity measurements

None of the previous studies of Alfvén waves in liquid metals that we know of, provided measurements of the fluid velocity. Here, we use ultrasound Doppler velocimetry as pioneered by Brito et al. (2001) in liquid sodium. There are several problems that render the measure particularly difficult: (i) the acquisition time must be as short as 10 ms to capture the wave; (ii) expected fluid velocities are only a few centimeters per second. Additional issues arise when the outer sphere spins: (iii) particles that scatter ultrasounds back to the probe become scarce as they get centrifuged; (iv) small unbalance of the rotating sphere creates signals at the rotation frequency and its overtones; (v) the electric signals to and from the embarked ultrasound probes pass through slip rings, where they get polluted by electromagnetic noise.

In order to measure angular velocities –the expected main component of our Alfvén waves– we shoot ultrasound beams from ports in the outer shell at 24° from the radial direction, as in Brito et al. (2011). We could retrieve satisfactory data from two beams, drawn in Figure 1a. Figure 9 shows the projection of their (straight) rays in an (s, z) plane, where s is the cylindrical radius. Drawn dots are separated by a constant distance along the ray of $0.1\, r_o$. Ray 1 is symmetric with respect to the equatorial plane, while ray 2 retains a constant latitude of $-20°$. To keep the acquisition time as short as possible, we measure fluid velocities only along a portion of the ray straddling its midpoint, which is closest to the inner sphere. We use the trigger mode of our Signal Processing DOP3010 ultrasound velocimeter to start the acquisition at the instant we trigger the jerk, which is in turn related to the actual

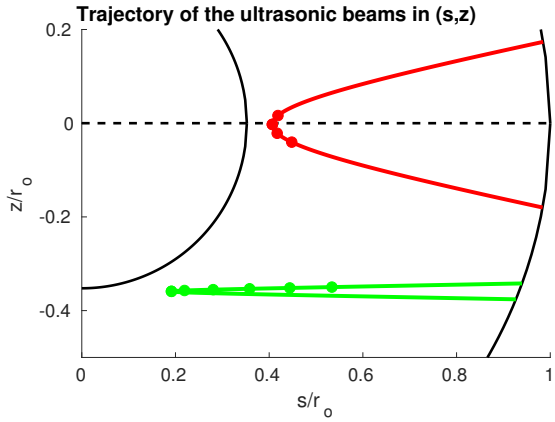

Figure 9. Projections of ultrasound rays 1 (red) and 2 (green) in the (s, z) plane of the DTS-Ω experiment. Dots are drawn at the midpoint of the ray, and every $0.1\, r_o$ away from it along the ray where data shown in Figure 10 is collected.

start of the jerk deduced from the torque of the inner sphere motor drive, as described in Appendix A.

Figure 10a shows a surface rendering of the Alfvén wave angular velocity as a function of time and distance along ultrasound ray 1, when the outer sphere is at rest ($f = 0$). We have stacked 5 records of jerks similar to those of sections 4.2 and 4.3, with $\Delta\varphi = 170^\circ \pm 9^\circ$ and $t_{rise} \simeq 55$ ms. The probed region only extends from a distance along the ray $d_{ray}/r_o = -0.13$ to 0.18 around the midpoint, and the time resolution is 16 ms. We see the rapid rise of the angular velocity at the Alfvén wave front, followed by a slow decrease. The peak velocity is slightly offset from the midpoint of the ray.

Synthetics of our measurements, computed from the same simulation as in sections 4.2 and 4.3, are shown in Figure 10c. We recall that this simulation uses the experimental jerk time-function, and has a reduced inner sphere conductivity. The siumulation shows a similar behaviour, with two important differences: (i) the maximum amplitude in our measurements is about twice smaller than simulated; (ii) measured velocities decay with time about 6 times more slowly than predicted.

Ray 2 looks more promising to probe the presence of the geostrophic velocity column that marks the constraint of rotation (see Figure 6). Symptomatic of the difficulties mentioned earlier, we could only get a handful of records for this ray geometry for $f = -10$ Hz. We stacked 8 jerks with $\Delta\varphi = 143^\circ \pm 1^\circ$ and $t_{rise} = 45$ ms. The result is shown in Figure 10b. The time resolution is 20 ms, but we had to to apply a 3 points median-filter in time to remove some spurious peaks at the rotation frequency.

The corresponding simulation synthetics are shown in Figure 10d, Again, the measured velocities

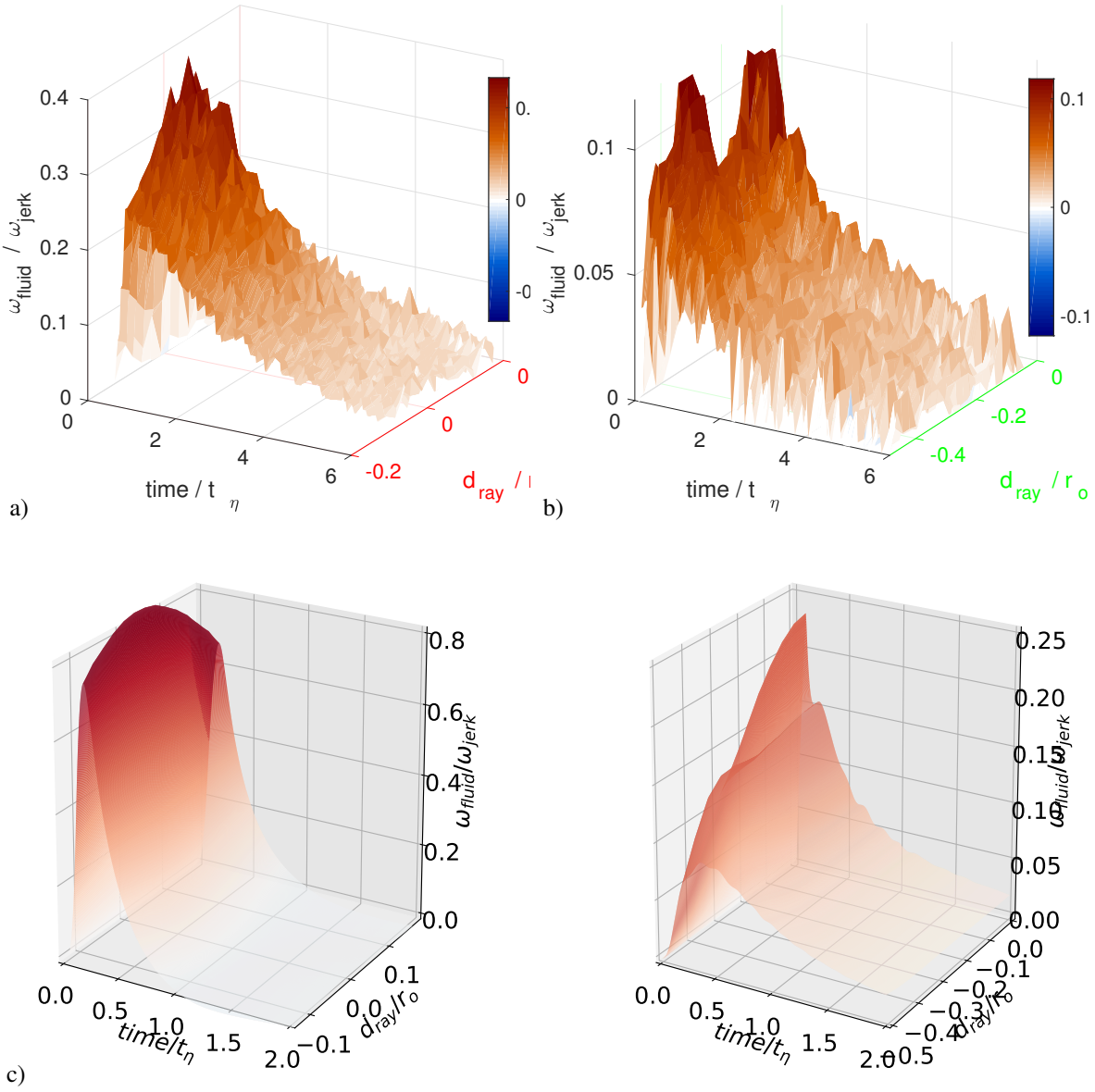

Figure 10. Color surface rendering of the fluid angular velocity ω_{fluid}, as a function of time (normalized by t_η) and distance along the ray (normalized by r_o), with $d_{ray} = 0$ at the midpoint of the ray. Angular velocities are normalized by $\Delta\varphi/t_{jerk}$. (a) Ray 1. Stack of 5 records for $f = 0$. (b) Ray 2. Stack of 8 records for $f = -10$ Hz. (c) Ray 1. Synthetics for $f = 0$, with the same parameters as in figure 5c. (d) Ray 2. Synthetics for $f = -10$ Hz.

are about twice smaller than simulated, and they do not peak at the same d_{ray}.

For the short ray portions we could measure, the synthetics do not show huge differences between the rotating versus non-rotating case. Overall, our harvest of velocity measurements is somewhat disappointing. On the sunny side, we obtain clear and reproducible signals that nicely show the sudden

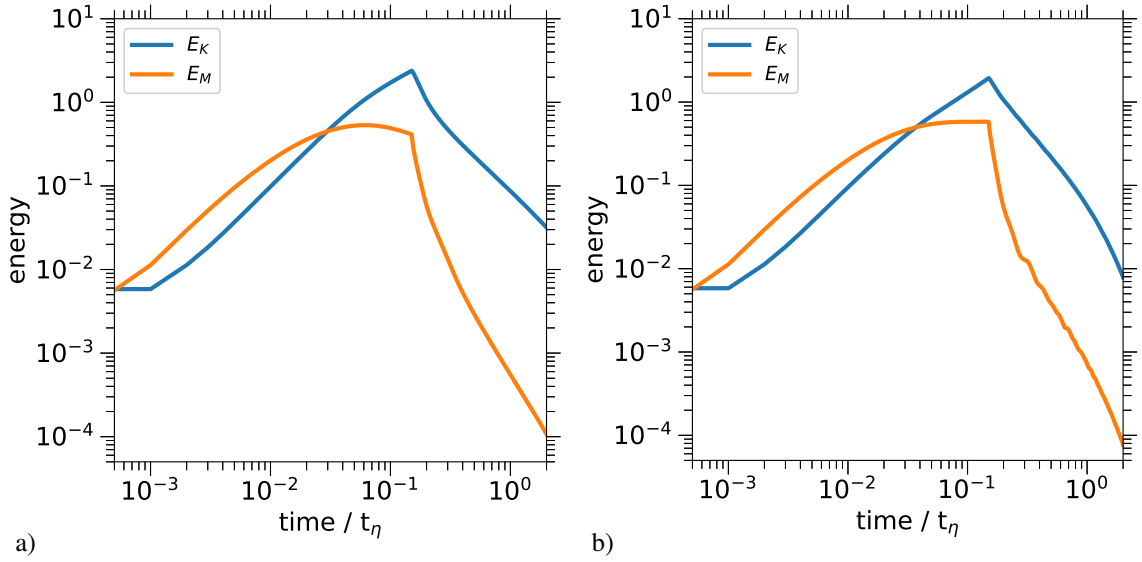

Figure 11. Log-log plots of the time-evolution of the kinetic (blue) and magnetic (orange) energies of Alfvén waves and torsional Alfvén waves from numerical simulations. (a) $f = 0$; (b) $f = 15$ Hz. Inner sphere jerks sweep a $\Delta\varphi = 90°$ angle. The jerk duration is $t_{jerk} = 0.15\, t_\eta$. Both E_M and E_K are normalized by $\rho r_o^5/t_\eta^2$.

rise and slow decay of angular velocity of the Alfvén and torsional Alfvén waves. On the dark side, our records do not clearly identify the influence of rotation, and the velocities we measure are about twice smaller than predicted. We think that the latter problem is due to coupling issues, which are discussed in Appendix C. Indeed, Table A1 indicates that the coupling was lower for these runs.

5 SCALING LAWS

We ran a series of numerical simulations with DTS-Ω parameters, varying the swept angle $\Delta\varphi$ from 1° to 180°, and the jerk duration t_{jerk} from 0.05 to 0.6 t_η. The time-function of the jerk rotation rate was a simple boxcar, and we set the magnetic Prandtl number to $Pm = 10^{-3}$. The electric conductivities were those of Table 2. The simulations covered both linear ($Re \ll 1$) and non-linear ($Re \gg 1$) regimes, without or with rotation, but all were axisymmetric.

5.1 Time evolution of the kinetic and magnetic energies

We integrate the energy densities over the volume of the spherical shell to obtain the total instantaneous kinetic $E_K(t)$ and magnetic $E_M(t)$ energies of the waves.

Figure 11 displays the time evolution of the kinetic and magnetic energies for simulations without rotation (left) and with rotation (right). Both jerks sweep a $\Delta\varphi = 90°$ angle with a boxcar time

function with $t_{jerk} = 0.15\, t_\eta$. We see that the kinetic and magnetic energies initially build up at similar rates, but that the magnetic energy levels off after $t \simeq 0.05\, t_\eta$ while the kinetic energy continues rising until the jerk stops. Magnetic energy is leaking out of the sphere because of magnetic diffusion while kinetic energy accumulates. After that, both energies decrease, magnetic energy decreasing more rapidly than kinetic energy.

In the absence of rotation, the damping reaches a power law, with $E_K \sim t^{-1.3}$ and $E_M \sim t^{-2.2}$, while exponents $-1/2$ and $-3/2$ were derived for the decay of turbulence by Alfvén waves in a uniform magnetic field by Moffatt (1967).

For torsional Alfvén waves, the behaviour is not strikingly different, but we observe that the energies decay exponentially with time rather than with a power law, in contrast with the results of Sreenivasan and Narasimhan (2017). The maximum magnetic energy is slightly larger than in the no-rotation case, yielding almost energy equipartition for the shortest jerks. The wiggles that show up in the magnetic energy curves are the magnetic signature of inertial waves.

5.2 Maximum energies

We now examine how the maximum magnetic E_M^{max} and kinetic E_K^{max} energies scale with the jerk parameters. Figure 12 compiles E_M^{max} versus Rm_{jerk}^2 for several numerical simulations and experiments. For the latter, we convert the BP5 (B_φ closest to the inner sphere) amplitude to E_M^{max}, assuming the same relationship as in the corresponding simulations. For all runs, we find that E_M^{max} is proportional to the square of the magnetic Reynolds number $Rm_{jerk} = U_{jerk} r_o/\eta$, irrespective of the Lehnert number and jerk duration. More specifically, expressing the energies in $\rho U_{jerk}^2 r_o^3$ units, we get: $E_M^{max} \simeq 5 \times 10^{-2}$.

We find that the E_K^{max}/E_M^{max} ratio increases almost linearly with t_{jerk} for torsional Alfvén waves, with $E_K^{max}/E_M^{max} \simeq 22\, t_{jerk}/t_\eta$, independent of Rm_{jerk}.

Reducing the conductivity of the inner sphere reduces the magnetic and kinetic energies of the wave. Finally, we note that the surface electric potentials follow the trend of the fluid velocity, confirming that they can be used as a proxy of the latter, as in section 4.3.

It is interesting to compare the kinetic and magnetic energies of Alfvén waves to their equivalent when the inner sphere spins at a constant rate Δf with respect to the outer sphere. Nataf (2013) and Cabanes et al. (2014a) report values obtained from global reconstructions of the mean axisymmetric velocity and magnetic fields in the DTS experiment. Both energies scale with $U^2 = (2\pi \Delta f r_i)^2$ at first order. Expressing the energies in $\rho U^2 r_o^3$ units, they range from $E_K \simeq 3.6$ and $E_M \simeq 1.6 \times 10^{-3}$ for $Rm = 3.5$ to $E_K \simeq 2.8$ and $E_M \simeq 3.5 \times 10^{-3}$ for $Rm = 10$, after converting to our definition of

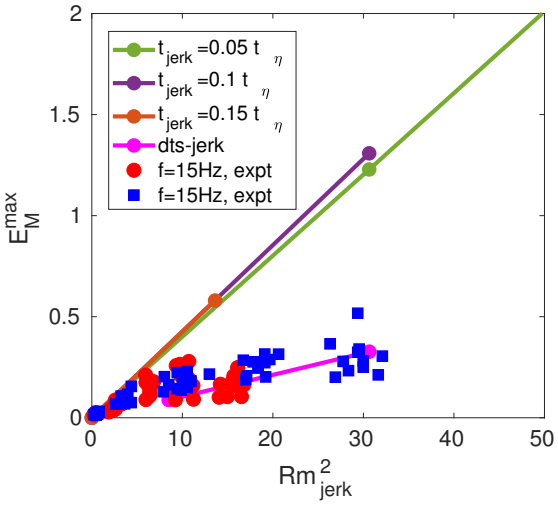

Figure 12. Evolution of the maximum magnetic energy E_M^{max} with Rm_{jerk}^2 in simulations (connected points) and experiments (symbols). The rotation rate is $f = 15$ Hz for all data shown, but non-rotating cases show a very similar behaviour. The curve labelled 'dts-jerk' uses $\sigma_i = \sigma_{Na}$ and a dts-jerk time function.

U. The magnetic energy of the waves is much larger than the magnetic energy achieved in the steady state. We can see this as the ability of the flow to adjust for limiting magnetic induction, as in Ferraro's law (Ferraro 1937).

6 DISCUSSION

We have presented the first experimental evidence for torsional Alfvén waves, *i.e.* geostrophic Alfvén waves, which obey the Proudman-Taylor constraint imposed by rapid rotation. We have measured both the induced azimuthal magnetic field inside the fluid shell (Figure 5) and the electric potentials at the surface of the container (Figure 8). The signature of rotation is best seen on surface electric potentials, which are sensitive to the velocity field through Ohm's law. The velocity field is indeed strongly modified by rotation, as shown by meridional maps of the azimuthal velocity field from numerical simulations (Figure 6). We have also performed the first measurements of the velocity perturbation associated with Alfvén waves, using ultrasound Doppler velocimetry (Figure 10), but we could not use them to clearly identify the role of rotation.

The effect of rotation also shows up in the magnetic waveforms we record (Figure 5). Indeed, the case with no rotation displays a negative overshoot, which is nearly absent in the rotating case. Numerical simulations (Figure 6) indicate that the negative overshoot if the signature of an Alfvén wave that originated in the opposite hemisphere, a consequence of the dipolar nature of the imposed

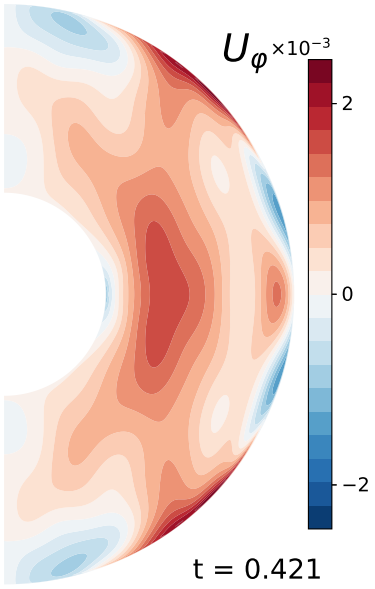

Figure 13. Inertial modes signatures in a meridional snapshot of azimuthal fluid velocity U_φ at time $t = 0.421\, t_\eta$ for a numerical simulation with $Pm = 10^{-5}$, $f = 15$ Hz, $\Delta\varphi = 1°$, boxcar jerk time-function with $t_{jerk} = 0.05\, t_\eta$.

magnetic field (see Figure 3). This phenomenon is best seen on snapshots of the meridional maps of the azimuthal magnetic field for simulations with a much reduced magnetic diffusion (Figure 7). Geostrophic Alfvén waves, which travel in the s-direction, do not show this phenomenon. However, magnetic diffusion introduces an additional twist in that case. The meridional map of the azimuthal velocity in Figure 6d, shows that the geostrophic cylinder is smeared. It extends back around the inner sphere, and persists after the end of the jerk, producing a weak reversed shear in that region, inducing a weak negative overshoot for the magnetic field.

With global rotation, both experiments and simulations show that sudden jerks trigger inertial waves in the fluid. In contrast with earlier studies dealing with the interaction of inertial waves with an imposed magnetic field (Moffatt 1967; Bardsley and Davidson 2016; Sreenivasan and Narasimhan 2017), waves encounter boundaries in our study. In doing so, they create geostrophic cylinders (Figure 6d), which are the key feature of torsional Alfvén waves. The interferences of other inertial waves build inertial modes, as best seen in Figure 13 and movie Up-15-modes.mp4.

The Lundquist number in our experiment is only 12 at the equator of the inner sphere, decreasing to 0.5 at the outer sphere. The effect of magnetic diffusion is therefore larger than in the sodium experiments of Jameson (1964), or in the gallium alloy experiments of Alboussiere et al. (2011), which both

reached $Lu = 60$. We note that the propagation velocity of the resulting damped Alfvén wave appears *larger* than that of ideal waves when we observe the signals in the time domain (Figure 4). We get the opposite answer when we compare the position of the wave in space, as illustrated by comparing Figures 6 ($Lu = 12$) and 7 ($Lu = 1200$). The core of the waves has travelled farther away in the latter case, while the snapshot is taken at a time three times shorter in Alfvén time units.

There are several properties of our set-up that make it interesting, besides the possibility to study the effect of rotation. As noted by Jameson (1964), the vertical walls of the container were responsible for a large dissipation in the early experiments (Lundquist 1949; Lehnert 1954a). In our set-up, Alfvén waves propagate freely from the inner sphere outwards, without meeting any wall, except for the inner sphere itself, were interesting reflexions do occur.

Another interesting feature of our set-up is the way we trigger the Alfvén wave by a jerk of the inner sphere. It produces simultaneously an azimuthal velocity impulse and an azimuthal magnetic field impulse, the latter being proportional to the imposed magnetic field. The simple and smooth geometry of the inner body permits quantitative comparisons with axisymmetric numerical simulations in spherical geometry. And we found indeed a good quantitative agreement between the experiments and the simulations for the amplitudes of the magnetic field and of surface electric potentials, provided we reduce the electric conductivity of the inner sphere from that of copper to that of sodium, because of coupling issues (see Appendix C).

Schaeffer and Jault (2016) emphasize the role of the electrical conductivity of the walls for inhibiting the reflexion of torsional waves when they reach the equator. They show that the reflexion coefficient R can be approximated by $R = \frac{1-Q-\sqrt{Pm}}{1+Q+\sqrt{Pm}}$, where $Q = V_A \delta_w / \eta_w$, for a wall of thickness δ_w and magnetic diffusivity η_w, with V_A the velocity of Alfvén waves near the wall. In our set-up, we get $Q \simeq 1$ so that torsional Alfvén waves would hardly reflect, were their amplitudes not heavily diminished by magnetic diffusion in the bulk.

Finally, we note that none of the diagnostics we used in the experiment (induced azimuthal magnetic field, surface electric potentials, *in situ* fluid velocities) is accessible in the study of torsional waves in the Earth's core. Instead, it is only the surface fluid velocities deduced from the magnetic field secular variation that enabled Gillet et al. (2010) to detect and study torsional waves in the core. This works well in the Earth because: (i) the Lundquist number is large enough ($Lu \sim 10^4$) for the frozen-flux approximation to be valid, (ii) the Lehnert number is small enough ($Le \sim 10^{-4}$)

for torsional waves to be really z-invariant. In the DTS-Ω experiment, we have recorded the 'secular variation' of the magnetic field at the surface, but magnetic diffusion prohibits using the frozen-flux approximation. Nevertheless, we might try to disentangle the effects of advection and diffusion in a follow-up study, as in Cabanes et al. (2014a).

ACKNOWLEDGMENTS

This work was funded by the French Agence Nationale de la Recherche under Grant N° ANR-13-BS06-0010 (TuDy). The XSHELLS code used for the numerical simulations is freely available at https://bitbucket.org/nschaeff/xshells. We thank Dr Aldo Figueroa for early numerical simulations, and Patrick Larizza, Jean-Paul Masson, Adeline Richard, and Dominique Grand (SERAS), for their invaluable contribution to the DTS-Ω set-up. ZT thanks Prof Ahcène Bouabdallah for his help and support, and the Ministry for Higher Education and Research of Algeria for support.

REFERENCES

Alboussiere, T., Cardin, P., Debray, F., La Rizza, P., Masson, J.-P., Plunian, F., Ribeiro, A., Schmitt, D., Sep. 2011. Experimental evidence of Alfven wave propagation in a Gallium alloy. Physics of Fluids 23 (9).

Alfvén, H., Oct. 1942. Existence of Electromagnetic-Hydrodynamic Waves. Nature 150, 405. URL `http://dx.doi.org/10.1038/150405d0`

Alfvén, H., Fälthammar, C.-G., 1963. Cosmical electrodynamics. Oxford Clarendon Press.

Bardsley, O. P., Davidson, P. A., 2016. Inertial–alfvén waves as columnar helices in planetary cores. Journal of Fluid Mechanics 805, R2.

Barik, A., Triana, S., Hoff, M., Wicht, J., 2018. Triadic resonances in the wide-gap spherical couette system. Journal of Fluid Mechanics 843, 211–243.

Braginsky, S., 1970. Torsional magnetohydrodynamics vibrations in the earth's core and variations in day length. Geomagn. Aeron. 10, 3–12.

Brito, D., Alboussiere, T., Cardin, P., Gagniere, N., Jault, D., La Rizza, P., Masson, J. P., Nataf, H. C., Schmitt, D., Jun. 2011. Zonal shear and super-rotation in a magnetized spherical Couette-flow experiment. Physical Review E 83 (6, 2).

Brito, D., Nataf, H.-C., Cardin, P., Aubert, J., Masson, J.-P., Dec. 2001. Ultrasonic Doppler velocimetry in liquid gallium. Experiments in Fluids 31 (6), 653–663.

Cabanes, S., Schaeffer, N., Nataf, H.-C., Oct. 2014a. Magnetic induction and diffusion mechanisms in a liquid sodium spherical Couette experiment. Physical Review E 90 (4).

Cabanes, S., Schaeffer, N., Nataf, H.-C., Oct. 2014b. Turbulence Reduces Magnetic Diffusivity in a Liquid Sodium Experiment. Physical Review Letters 113 (18).

Cabanes, S., Schaeffer, N., Nataf, H.-C., Oct 2015. Erratum: Turbulence reduces magnetic diffusivity in a

liquid sodium experiment [phys. rev. lett. 113, 184501 (2014)]. Phys. Rev. Lett. 115, 189901.
URL https://link.aps.org/doi/10.1103/PhysRevLett.115.189901

Cardin, P., Brito, D., Jault, D., Nataf, H.-C., Masson, J. P., 2002. Towards a rapidly rotating liquid sodium dynamo experiment. Magnitnaya Gidrodinamika 38, 177–189.

Ferraro, V. C., 1937. The non-uniform rotation of the sun and its magnetic field. Monthly Notices of the Royal Astronomical Society 97, 458.

Figueroa, A., Schaeffer, N., Nataf, H. C., Schmitt, D., Feb. 2013. Modes and instabilities in magnetized spherical Couette flow. Journal of Fluid Mechanics 716, 445–469.

Gillet, N., Jault, D., Canet, E., Fournier, A., May 2010. Fast torsional waves and strong magnetic field within the Earth's core. NATURE 465 (7294), 74–77.

Gillet, N., Jault, D., Finlay, C. C., Jun. 2015. Planetary gyre, time-dependent eddies, torsional waves, and equatorial jets at the Earth's core surface. Journal of Geophysical Research-Solid Earth 120 (6), 3991–4013.

Gillet, N., Schaeffer, N., Jault, D., 2012. Rationale and geophysical evidence for quasi-geostrophic rapid dynamics within the earth's outer core. Physics of the Earth and Planetary Interiors 202-203, 78 – 88.
URL http://www.sciencedirect.com/science/article/pii/S0031920112000520

Jameson, A., Aug. 1964. A demonstration of Alfvén waves Part 1. Generation of standing waves. Journal of Fluid Mechanics 19 (4), 513–527.
URL http://www.cambridge.org/core/journals/journal-of-fluid-mechanics/article/demonstration-of-alfven-waves-part-1-generation-of-standing-waves/1F0D765B76D334560BC78C8A551E3B67

Jault, D., Jan. 2008. Axial invariance of rapidly varying diffusionless motions in the Earth's core interior. Physics of the Earth and Planetary Interiors 166 (1-2), 67–76.

Jault, D., Finlay, C., 2015. Waves in the core and mechanical core-mantle interactions. In: G. (ed.-in chief), S., P, O. (Eds.), Treatise on Geophysics, 2nd Edition. Vol. 8, Core Dynamics. Elsevier, Oxford, pp. 225–244.

Kaplan, E., Nataf, H.-C., Schaeffer, N., 2018. Dynamic domains of the derviche tourneur sodium experiment: Simulations of a spherical magnetized couette flow. Physical Review Fluids 3 (3), 034608.

Lehnert, B., 1954a. Magneto-Hydrodynamic Waves in Liquid Sodium. The Physical Review, 815–824.

Lehnert, B., 1954b. Magnetohydrodynamic waves under the action of the coriolis force. The Astrophysical Journal 119, 647–654.

Lundquist, S., 1949. Experimental Investigations of Magneto-Hydrodynamic Waves. Physical Review 76 (12), 1805–1809.
URL https://journals-aps-org/pr/abstract/10.1103/PhysRev.76.1805

Moffatt, H. K., 1967. On the suppression of turbulence by a uniform magnetic field. Journal of Fluid Mechanics 28 (3), 571–592.

Nataf, H.-C., Mar. 2013. Magnetic induction maps in a magnetized spherical Couette flow experiment. Comptes Rendus Physique 14 (2-3), 248–267.

Nataf, H. C., Alboussiere, T., Brito, D., Cardin, P., Gagniere, N., Jault, D., Masson, J. P., Schmitt, D., Oct.

2006. Experimental study of super-rotation in a magnetostrophic spherical Couette flow. Geophysical and Astrophysical Fluid Dynamics 100 (4-5), 281–298.

Nataf, H. C., Alboussiere, T., Brito, D., Cardin, P., Gagniere, N., Jault, D., Schmitt, D., Sep. 2008. Rapidly rotating spherical Couette flow in a dipolar magnetic field: An experimental study of the mean axisymmetric flow. Physics of the Earth and Planetary Interiors 170 (1-2), 60–72.

Roberts, P. H., 1967. An introduction to magnetohydrodynamics. Longmans.

Schaeffer, N., Mar. 2013. Efficient spherical harmonic transforms aimed at pseudospectral numerical simulations. GEOCHEMISTRY GEOPHYSICS GEOSYSTEMS 14 (3), 751–758.

Schaeffer, N., Jault, D., May 2016. Electrical conductivity of the lowermost mantle explains absorption of core torsional waves at the equator. Geophysical Research Letters 43 (10), 4922–4928.

Schaeffer, N., Jault, D., Cardin, P., Drouard, M., 2012. On the reflection of alfvén waves and its implication for earth's core modelling. Geophysical Journal International 191 (2), 508–516.
URL http://dx.doi.org/10.1111/j.1365-246X.2012.05611.x

Schmitt, D., Alboussiere, T., Brito, D., Cardin, P., Gagniere, N., Jault, D., Nataf, H. C., Jun. 2008. Rotating spherical Couette flow in a dipolar magnetic field: experimental study of magneto-inertial waves. Journal of Fluid Mechanics 604, 175–197.

Schmitt, D., Cardin, P., La Rizza, P., Nataf, H. C., Feb. 2013. Magneto-Coriolis waves in a spherical Couette flow experiment. European Journal of Mechanics B-Fluids 37, 10–22.

Siso-Nadal, F., Davidson, P. A., 2004. Anisotropic evolution of small isolated vortices within the core of the earth. Physics of Fluids 16 (5), 1242–1254.

Sommeria, J., Moreau, R., 1982. Why, how, and when, mhd turbulence becomes two-dimensional. Journal of Fluid Mechanics 118, 507–518.

Spruit, H. C., Jan 1982. Propagation speeds and acoustic damping of waves in magnetic flux tubes. Solar Physics 75 (1), 3–17.
URL https://doi.org/10.1007/BF00153456

Sreenivasan, B., Narasimhan, G., 2017. Damping of magnetohydrodynamic waves in a rotating fluid. Journal of Fluid Mechanics 828, 867–905.

Supplementary material

Supplementary movies Up-0.mp4, Bp-0.mp4, Up-15.mp4, Bp-15.mp4, and Up-15-modes.mp4 are available at xxx.

Appendices

APPENDIX A: TRACKING JERKS OF THE INNER SPHERE

In order to better describe the source of our Alfvén waves, we need to retrieve a few properties of the impulsive inner sphere rotation achieved in our DTS-Ω experiment. We produce this 'jerk' by ordering a sudden jump of the rotation rate to the motor driving the inner sphere, followed by a sudden drop to its original value. We do not control the exact timing of these two orders, and therefore, we obtain jerks of various sizes. In this appendix, we describe how we retrieve the two properties needed to compare with simulations: the total angle $\Delta\varphi$ swept by the inner sphere (in the rotating frame) and the jerk time-function.

A1 Obtaining $\Delta\varphi$

We use two different methods to measure $\Delta\varphi$, depending on whether the outer sphere is at rest (Alfvén waves) or spins (torsional Alfvén waves). The $\Delta\varphi$ produced by our jerks range from 10° to 190°.

A1.1 obtaining $\Delta\varphi$ for Alfvén waves

Figure A1a shows magnetic field records for a succession of 8 inner sphere jerks, when the outer sphere is at rest. The three components B_r, B_θ, B_φ are measured (in a sleeve) $\sim$ 20 mm above the surface of the inner sphere. The dipole field has been subtracted. The jerks show up as very thin impulses, separated by long plateaus of different heights. During a jerk, the inner sphere changes from angular position φ_0 to $\varphi_0 + \Delta\varphi$ with respect to the outer sphere (hence the sleeve). The plateaus indicate that the magnetic field produced by the inner magnet is not perfectly axisymmetric. In fact, this property was used by Cabanes et al. (2014b, 2015) to probe the effective magnetic diffusivity in DTS, and Cabanes et al. (2014a) provide the scalar magnetic potential of this non-axisymmetric component (see their figure 13a). The combination of the height of the plateaus for the 3 B-components unequivocally characterizes the angular position of the inner sphere, hence the $\Delta\varphi$ angle swept by the inner sphere during a jerk.

A1.2 obtaining $\Delta\varphi$ for torsional Alfvén waves

We use a different method when the outer sphere spins. We can time precisely when the outer sphere reference longitude matches the lab frame reference, and similarly for the inner sphere. This provides the rotation rates of both spheres. We can also determine the time delay, and hence the phase lag,

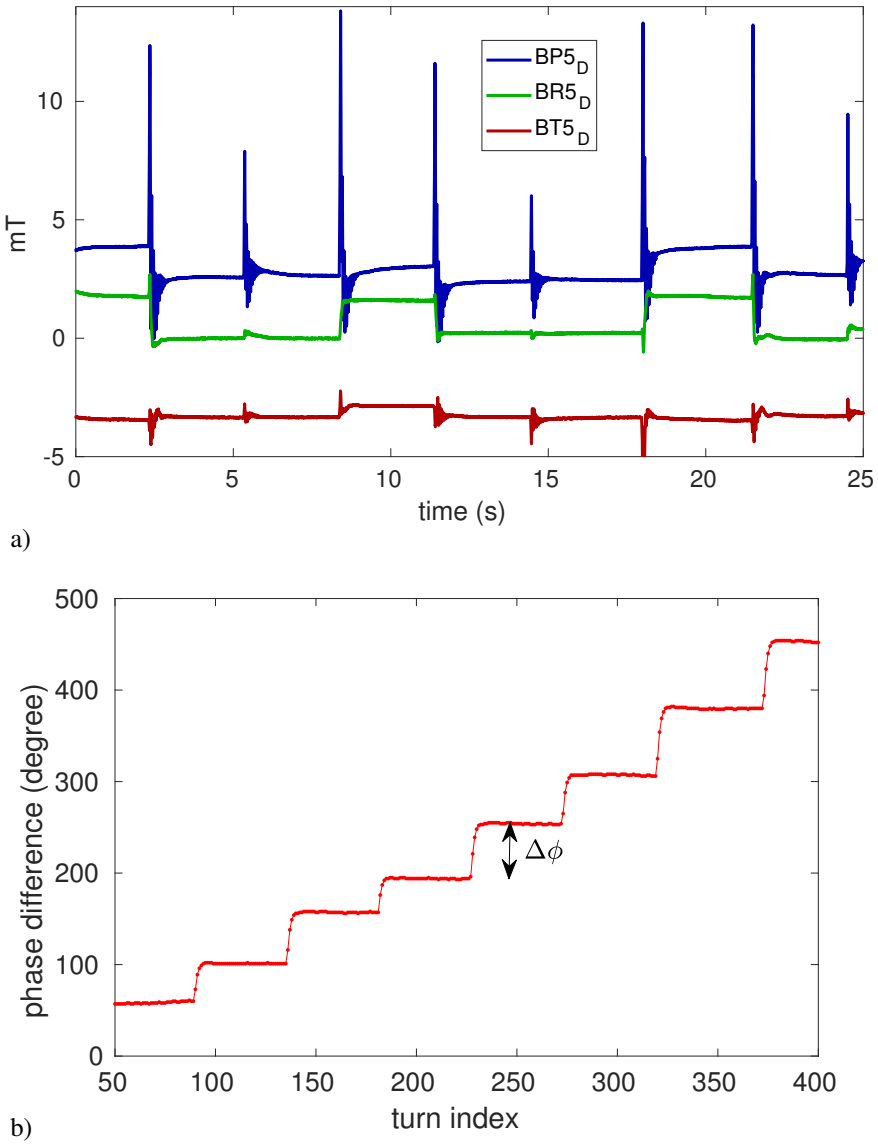

Figure A1. Determination of the angle $\Delta\varphi$ swept by each jerk. (a) no rotation case: the figure shows the 3 components $(B_r, B_\theta, B_\varphi)$ of the induced magnetic field close to to the inner sphere as a function of time. Eight jerks are visible. $\Delta\varphi$ is obtained from the difference between the inner sphere longitudes after and before each jerk, deduced from their specific $(B_r, B_\theta, B_\varphi)$ combination. (b) rotating case ($f = 15$ Hz): the longitude difference between the inner sphere and the outer sphere is plotted as a function of the turn index of the outer sphere. A constant residual drift of the inner sphere of about $1°$/turn has been subtracted. The figure illustrates how $\Delta\varphi$ is retrieved for each jerk.

between the two spheres at each turn. Figure A1b illustrates the determination of $\Delta\varphi$ for a subset of 7 inner sphere jerks for $f = 15$ Hz.

A2 Jerk time-function

The first thing is to get the precise starting time of each jerk. We obtain this from the record of the torque applied to the inner sphere provided by its motor drive. It rises abruptly from some initial value to values in excess of 100 Nm, and we can pin-point the rise start with a precision of about 1 ms. It drops very abruptly as well, and we pin-point the time at which it crosses its initial level to within 1 ms as well. This defines the rise time t_{rise} of the jerk. It ranges from 15 to 60 ms.

The motor drive also provides the instantaneous rotation rate $\Delta f(t)$ of the motor. Figure A2 displays a typical record of that signal. It is somewhat noisy, but one clearly sees a linear rise between the two vertical lines that mark the rise and fall of the torque. It is followed by a quasi-exponential decay, with a time constant $t_{decay} \simeq 75$ ms. Knowing the total angle $\Delta\varphi$ of the jerk from our previous analysis, we can calculate the peak rotation rate Δf_{max} by the integration of this rise-and-decay time-function. We get:

$$2\pi\Delta f_{max} = \frac{\Delta\varphi}{t_{decay} + t_{rise}/2}. \tag{A.1}$$

Figure A2 shows that the synthetic jerk time-function thus obtained provides a good fit. We define $t_{jerk} = t_{decay} + t_{rise}/2$. We implemented this time-function in the simulations.

Δf_{max} is used in the estimate of the magnetic Reynolds number of the jerk: $Rm_{jerk} = r_o U_{jerk}/\eta$, with $U_{jerk} = 2\pi\Delta f_{max} r_i = r_i \Delta\varphi / t_{jerk}$.

APPENDIX B: OSCILLATIONS OF THE INNER SPHERE

The above procedure provides the jerk time-function of the pulley that drives the inner sphere of DTS-Ω. However, the pulley entrains the inner sphere through a magnetic coupler. Sudden jerks create a small phase lag $\delta\varphi_{lag}$ between the pulley and the inner sphere, which we can estimate from the time lag t_{lag} of the observed magnetic signal compared to our simulation (see section 4.1):

$$\delta\varphi_{lag} = 2\pi \int_0^{t_{lag}} \Delta f(t) dt = \frac{2\pi\Delta f_{max}}{t_{rise}} \frac{t_{lag}^2}{2}, \tag{B.1}$$

where Δf_{max} is calculated in Appendix A2. We get $\delta\varphi_{lag} \simeq 1.2°$.

The magnetic coupler-inner sphere system then behaves as a damped oscillator, with a characteristic frequency $\nu_{osc} \simeq 18$ Hz. The actual jerk waveform thus combines the pulley time-function and the oscillations resulting from the magnetic coupler, which have a clear signature on the measured magnetic (Figures 5ab) and electric (Figures 8ab) signals.

We have not included these oscillations in our simulations, but we can estimate their expected

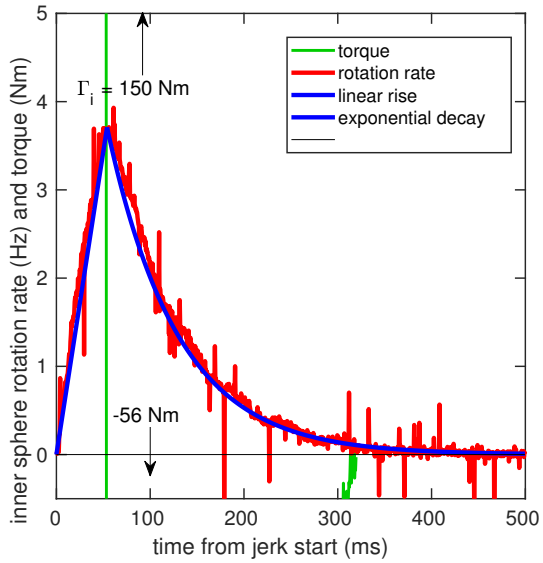

Figure A2. Typical time-function of a jerk in DTS-Ω. The figure displays the torque (green curve in Nm) and differential rotation rate (red curve in Hz) of the inner sphere motor drive during a jerk, for $f = 15$ Hz. The sudden rise of the torque to a value of about 150 Nm (off scale) yields the jerk origin time. The rotation rate increases linearly until the torque suddenly drops to negative values, here at about 50 ms after the jerk start. This defines t_{rise} for this jerk. Then, the differential rotation rate decreases exponentially back to zero, with $t_{decay} \simeq 75$ ms. This jerk swept an angle $\Delta\varphi \simeq 135°$. The blue piecewise curve is the synthetic jerk we use in the numerical simulations.

signature from our scaling laws. The magnetic Reynolds number of the oscillations is:

$$Rm_{osc} = \frac{2\pi\, \nu_{osc}\, \delta\varphi_{lag}\, r_i\, r_o}{\eta} \simeq 0.42. \tag{B.2}$$

This is about 13 times smaller than the magnetic Reynolds number of the jerks selected in Figure 5ab. We should find the same ratio between the signature of the oscillations and the jerk's main signal, since the scaling laws we found in section 5 predict that B is proportional to Rm. This is roughly what we find. The oscillations are slightly smaller for the electric potentials, consistent with an expected additional $\sqrt{t_{osc}/t_{rise}} \simeq 0.5$ factor.

APPENDIX C: COUPLING ISSUES

As in the early experiments of Lehnert (1954a), our Alfvén waves are produced by a shearing of the magnetic field lines at the copper-sodium interface at the inner sphere surface. The electric coupling between the liquid sodium and the copper inner shell therefore plays a crucial role. During its 12 years of operation, the DTS experiment has seen its coupling vary substantially, for reasons which have not been really understood. While it was good and stable in the experiments reported on by Brito et al.

[h]

Fig #	f Hz	$\Delta\varphi$ $^\circ$	t_{rise}/t_η	coupling	$Le(r_o)$	Rm_{jerk}
2ab,12c	15	14-190	0.04-0.12	0.5	0.011	0.5-5.6
4ab	15	110 ± 20	0.08	0.5	0.011	2.9
5a,8a	0	155 ± 25	0.1	0.5	∞	~ 4.9
5b,8b	15	155 ± 25	0.1	0.5	0.011	~ 4.9
10a	0	167-185	0.1	0.1	∞	~ 5.6
10b	-10	143	0.08	0.15	0.017	~ 4.6
A1a	0			0.5	∞	
A1b	15			0.5	0.011	
A2	15	135	0.1	0.5	0.011	4.2

Table A1. Parameters of the experiments. $Le(r_o)$ is the Lehnert number of equation 10 evaluated using the intensity of the magnetic field at the equator of the outer shell ($r = r_o$). Rm_{jerk} is the magnetic Reynolds number of the jerk. 'coupling' is the ratio of the measured ΔV_{-40} over its value simulated with an inner sphere with copper electric conductivity.

(2011), Schmitt et al. (2013), Nataf (2013) and Cabanes et al. (2014a,b, 2015), it was partly impaired in those of Nataf et al. (2006, 2008) and Schmitt et al. (2008). The coupling was good again in the first runs of the upgraded version DTS-Ω, but it deteriorated and remained imperfect even after a complete replacement of our sodium performed in September 2016.

However, Nataf et al. (2008) show that surface electric potentials provide a good proxy for the quality of the coupling for a given differential rotation rate. In order to get the good quantitative agreement between our measurements and our numerical simulations shown in Figures 5 and 8, we had to reduce the conductivity of the inner sphere shell from that of copper to that of liquid sodium in the numerical simulations. The coupling was not as good when we succeeded obtaining the ultrasound Doppler velocity profiles shown in Figure 10, with ΔV_{40} electric potentials 3 to 5 times smaller. Note that some coupling inhomogeneity between the upper and lower hemispheres is also revealed by the electric potentials in some cases.

APPENDIX D: EXPERIMENTAL AND NUMERICAL PARAMETERS

Table A1 summarizes the parameters of the experiments and Table A2 those of the numerical simulations presented in this article.

[h]

Fig #	f Hz	$\Delta\varphi$ $^\circ$	t_{rise}/t_η	jerk time -function	σ_i/σ_{Na}	$Lu(r_i)$	Pm	ℓ_{max}	NR
4cd	15	90	0.08	dts	1	12	10^{-4}	300	1000
5c,8c,6ac,10c	0	180	0.1	dts	1	12	10^{-4}	300	1000
5d,8d,6bd	15	180	0.1	dts	1	12	10^{-4}	300	1000
10d	-10	180	0.1	dts	1	12	10^{-4}	300	1000
			t_{jerk}/t_η						
7ac	0	0.1	2×10^{-4}	boxcar	4.2	1200	10^{-3}	120	550
7bd†	15	0.1	2×10^{-4}	boxcar	4.2	1200	10^{-1}	460	1200
11abd	0,15	90	0.05,0.15	boxcar	4.2	12	10^{-3}	120	550
12abd	0,15	1-180	0.05-0.6	boxcar	4.2	12	10^{-3}	120	550

Table A2. Parameters of the numerical simulations. The 'dts' jerk time-function is described in Appendix A2. σ_i is the electric conductivity of the shell housing the magnet of the inner sphere, while σ_{Na} is the electric conductivity of liquid sodium. The σ_i/σ_{Na} ratio is 4.2 for a copper shell. $Lu(r_i)$ is the Lundquist number of equation 11 evaluated using the intensity of the magnetic field at the equator of the inner sphere ($r = r_i$). ℓ_{max} is the maximum harmonic degree of the simulation, and NR the number of radial grid points. †This simulation had $r_o = 21$ m in order to get the same Elsasser number as in the experiment at 15 Hz, implying a Lehnert number 100 smaller than in the experiment.